Multivariate analysis of Visible and Infrared Thermal Imaging Spectrometer (VIRTIS) Venus Express nightside and limb observations

Stéphane Erard, Pierre Drossart, Giuseppe Piccioni

To cite this version:

Stéphane Erard, Pierre Drossart, Giuseppe Piccioni. Multivariate analysis of Visible and Infrared Thermal Imaging Spectrometer (VIRTIS) Venus Express nightside and limb observations. Journal of Geophysical Research. Planets, 2009, 114, 10.1029/2008JE003116 . hal-03785558

HAL Id: hal-03785558
https://hal.science/hal-03785558

Submitted on 25 Sep 2022

JOURNAL OF GEOPHYSICAL RESEARCH, VOL. 114, E00B27, doi:10.1029/2008JE003116, 2009

Multivariate analysis of Visible and Infrared Thermal Imaging Spectrometer (VIRTIS) Venus Express nightside and limb observations

S. Erard,[1] P. Drossart,[1] and G. Piccioni[2]

Received 14 February 2008; revised 31 May 2008; accepted 3 November 2008; published 7 January 2009.

[1] Spectral signatures measured by Visible and Infrared Thermal Imaging Spectrometer (VIRTIS) on the nightside and at the limb of Venus are analyzed with Independent Component Analysis. A methodology has been set up to minimize instrumental effects and to interpret the results on the basis of studies of the most common situations in the data set. The main spectral components commonly retrieved on the nightside include the bulk signal modulated by atmospheric opacity variations, photometric variations in the long-wavelength atmospheric windows, a branching parameter describing particle size variations, and O_2 emission at 1.26 and 1.58 μm. Faint atmospheric windows are detected at 1.51, 1.55, 1.78, and 1.82 μm for the first time. The polar vortex structure is outlined, with two main circular areas made of many concentric rings with alternating particle sizes. Discrete clouds about 100 km across are observed in low opacity conditions. High-altitude, warm clouds are tentatively observed from the polar vortex down to 55°S. At the limb, the two signatures of CO_2 nonlocal thermodynamic equilibrium emission are directly mapped, and the thermal structure of the cloud layers and upper atmosphere is apparent. Surface emission is detected with a spatial resolution limited by atmosphere blurring, reaching ~35 km in exceptional conditions. Horizontal offsets indicate that the radiation propagates mostly vertically, consistent with the large optical depth and vertical extent of the cloud layer. Intense scattering is suspected to take place at the bottom of the atmosphere, at least in the southern plains.

Citation: Erard, S., P. Drossart, and G. Piccioni (2009), Multivariate analysis of Visible and Infrared Thermal Imaging Spectrometer (VIRTIS) Venus Express nightside and limb observations, *J. Geophys. Res.*, *114*, E00B27, doi:10.1029/2008JE003116.

1. Introduction

[2] Early space observations of Venus have shown that the atmosphere is stratified in three main cloud layers which differ in particular in terms of scattering effects related to different particle density and size. Particle sizes aggregate around three modal values ranging from 0.6 μm (mode 1, forming a haze above the main cloud deck) to 7 μm (mode 3, dominant source of opacity in the lower/middle clouds). Mode 2 and 2′ particles (~2 and 3 μm in size) are present mostly in the upper and lower/middle clouds respectively, and make them uniformly opaque and relatively featureless spectrally at infrared wavelengths [e.g., *Esposito et al.*, 1983; *Grinspoon et al.*, 1993].

[3] The radiance of Venus' nightside is dominated by black body emission of the upper clouds longward of 3.5 μm, in the 70–75 km altitude range. CO_2 absorption and strong scattering by the haze and clouds blocks thermal emission from lower, warmer layers, except in discrete spectral windows where intensity peaks are observed. The shape of these peaks is influenced by specific species at specific altitudes, and by scattering effects. Signatures from various atmospheric layers are therefore present at various wavelengths, with spatial distributions related to the dynamics or absorbers in these layers [e.g., *Allen and Crawford*, 1984; *Carlson et al.*, 1991].

[4] Most notably, peaks centered at 1.02, 1.10, 1.18, and 1.28 μm are dominated by the emission of the very deep atmosphere and of the surface itself. Longer-wavelength peaks are strongly modulated by the atmospheric layers opacity, and allow tracking cloud motions in these layers [*Baines et al.*, 2006]. Increased radiance at 1.74 μm and 2.2–2.5 μm is thus indicative of opacity in the lower and middle clouds region (47–57 km); a smaller and narrower peak is also present at 1.31 μm. The ratio of peak intensities at 2.3, 1.74, and 1.31 μm is on the first-order a measurement of scattering effects, most notably related to particle size. Spatial variations in these ratios define latitudinal zones with different size distributions (mode 2 and mode 3 particle abundances [*Carlson et al.*, 1993]).

[5] H_2O in deeper layers affects the range from 1.10 to 1.19 μm, and therefore modifies the profile of the 1.10 and 1.18 μm peaks. H_2O at higher altitudes (~35 km) affects the intensity of the 1.74 μm peak. The wide 2.2–2.5 μm structure is sensitive successively to H_2O, CO, HF, OCS, and SO_2 in the 35–50 km altitude range [e.g., *Pollack et al.*, 1993]. Deexcitation of O_2 at 1.27 μm forms a rapidly varying airglow at ~95 km altitude, centered around the antisolar point, and overlapping the 1.28 μm window

---

[1] LESIA, Observatoire de Paris, CNRS Meudon, France.
[2] INAF, IASF, Rome, Italy.

0148-0227/09/2008JE003116

[*Connes et al.*, 1979]. Finally, thermal emission from the surface is expected to contribute to the first three peaks (at 0.98, 1.10 and 1.18 μm) and is controlled by surface elevation [e.g., *Meadows and Crisp*, 1996]. Lower areas are warmer, which translates in larger intensity in the short-wavelength peaks whenever atmospheric opacity is moderate enough to allow the signal to cross the entire path length.

[6] Visible and Infrared Thermal Imaging Spectrometer (VIRTIS) limb observations allow measurement of high-altitude emission from various species [*Drossart et al.*, 2007b]. These include CO_2 and CO fluorescence [*Gilli et al.*, 2008], deexcitation of O_2 recombined on the nightside [*Gérard et al.*, 2008], and OH emission in the so-called Meinel bands [*Piccioni et al.*, 2008]. In addition to the 1.27 μm band observed in nadir view another, a much fainter O_2 feature is located at 1.58 μm and can be observed at the limb [*Piccioni et al.*, 2008]. Nonlocal thermodynamic equilibrium (non-LTE) emission of CO_2 is also observable at the limb depending on the Sun direction, with a significant magnitude in the 4.25–4.5 μm range and additionally at 2.7 and 2.0 μm. CO has a similar emission feature in the 4.6–4.7 μm range. Finally, the very faint OH bands have been observed in some situations in the 1.42–1.46 μm and 2.7–3.1 μm ranges [*Piccioni et al.*, 2008].

[7] The clouds are organized in zonal bands with elongated features at midlatitudes up to the polar vortex area, with occasional latitudinal mixing [*Piccioni et al.*, 2007]. Mottled, irregular and warped turbulent structures are present at lower latitudes, and packets of gravity waves are detected at different latitudes in the upper and lower clouds [*Sanchez-Lavega et al.*, 2008]. Poleward of 75°S, the polar vortex is observed with its characteristic dipole pattern displaced from the pole, and surrounded by a dark, cold cloud collar extending down to 60°S [*Piccioni et al.*, 2007]. This is the counterpart of a similar structure observed in the northern hemisphere by Pioneer Venus [*Taylor et al.*, 1979].

[8] The spectral signatures measured by VIRTIS on the nightside are hereafter analyzed with Independent Component Analysis (ICA) to determine their spectral associations and spatial regularities. These phenomena are usually studied through simple spectral parameters such as peak intensities measured at a given wavelength. The use of ICA is expected to improve data analysis for three reasons:

[9] 1. Increased signal-to-noise ratio. Multivariate analyses take advantage of the complete peak profiles, not only the central wavelength; besides, they gather together all peaks with a consistent spatial distribution, which further enlarges the signal.

[10] 2. Intrinsic spectral parameter corrections. Opposition between measurements at different wavelengths is similar to computing more elaborate spectral parameters, e.g., stray light removal, band depth computation by subtracting a local continuum, removal of a background cloud pattern.

[11] 3. Optimized spectral associations. The ICA evidences associations of spectral measurements in a more robust and flexible way than correlation between peak intensities, for instance. Given enough spectra and variability, associated signatures correspond to the same physical phenomenon.

[12] A practical problem is raised by the increasing capacities of modern imaging spectroscopy experiments. The data sets have become so large that they are difficult to analyze, especially because the new and interesting information consists in small and local signatures hidden inside highly correlated spectral data, and carry very little variance. For the above reasons, ICA may offer a practical way to analyze such large data sets, at least as a quick-look tool, with an ability both to identify the major spectral types in the data, and to extract minor but markedly different signatures.

[13] The objectives of this work are therefore to assess the capacities of the method to study a thick planetary atmosphere, to identify the type of preprocessing potentially required, and to create a methodology to interpret the results. This involves (1) identifying the main associations observed in typical situations on Venus, (2) studying small signatures carrying little variance and observed with low signal-to-noise ratio, and (3) assessing the effects of noise, random events, and remaining instrumental effects in the data. The present work focuses on the overall regularities encountered so far in the VIRTIS data set, and will be used in future works as a general frame to analyze unusual situations.

2. Method

2.1. Principle of the Analysis

[14] ICA is a multivariate method which is focused on signal unmixing (blind source separation). Like Principal Components Analysis (PCA) it starts from mixed signals only, and returns a set of components and mixing coefficients [*Comon*, 1990]. In contrast to PCA though, it does not look for the directions of maximal variance, but it searches for independent components. Statistical independence implies an absence of correlation, but is a more stringent condition: it means that the distribution of one variable does not tell anything about the distribution of the other variables (marginal probability distribution functions are separable).

[15] Technically, this is done in two steps: first, the data are decorrelated and scaled (whitened); this is achieved by projecting the data in their eigenspace, or in its first dimensions. Second, ICA searches a rotation of this subspace that maximizes a measure of non-Gaussianity, because any mixture of independent components is expected to be more Gaussian than the individual components; this however assumes that at most one component has a Gaussian probability distribution function. Several solutions have been implemented, using various non-Gaussianity estimates. In this paper, we use the JADE algorithm [*Cardoso*, 1999], which is based on joint diagonalization of the fourth-order cumulant tensor. JADE has some practical advantages over other ICA algorithms, in particular it is more efficient (less demanding in terms of CPU time) and it uses direct computation (not starting from random nuclei), which makes the results reproducible from one run to the next. As all ICA algorithms however, JADE can only identify directions in the data space but does not provide their relative magnitudes. More explicitly, ICA defines a transform:

$$X = \mathbf{A}S \tag{1}$$

where X is the data, S is independent components, and A is the matrix of mixing coefficients. ICA identifies A and S from X alone, but only the products A × S can be identified. Like most ICA algorithms, JADE scales the signals S so that their variance equals one. As a consequence, the signs of the returned components are arbitrary; in addition, they are ordered according to a non-Gaussianity parameter, not according to their contributions to the data. Results can be refined using extra knowledge of the physical problem involved. The only free parameter in ICA is the number of components retained in the first step.

[16] ICA has been increasingly used in the recent years. Although originally applied to observational cosmology, it has proven particularly well adapted to analysis of planetary remote sensing data [e.g., *Forni et al.*, 2005; *Moussaoui et al.*, 2008]. Experimentally, applications of ICA to spectral cubes are more precise and easier to interpret than PCA: independent components are closer to physical associations of variables than principal components; ICA clearly separates components introducing similar variance in the data set, whereas PCA does a terrible job at inverting signal mixtures in these conditions; for the same reason, independent components with limited spatial exposure (and therefore limited weight) are readily identified, whereas PCA usually fails to identify these small variations; finally, ICA is by construction very robust to random noise in the data, which can be considered Gaussian; in contrast, a simple PCA does not separate low-variance signals from noise and often ascribes a higher weight to noisy components than to physical phenomena with minor expression. The Maximum Noise Fraction method, which is essentially a PCA applied to noise-whitened data, reduces this problem but does not appear as efficient as ICA in this context.

2.2. Implementation for VIRTIS

[17] ICA is hereafter applied to spatially extended data from the infrared imaging channel, VIRTIS M-IR. VIRTIS-M data are organized in spectral cubes, with one spatial dimension and the spectral dimension acquired simultaneously at each time step using bidimensional detectors [*Coradini et al.*, 1998; *Drossart et al.*, 2007a]. The spectral range (1.02–5.12 μm) is sampled with a constant spectral step of 9 nm, and an actual channel width of ~16.5 nm. The image dimension and the spatial resolution depend on slant distance and binning mode. The noise equivalent radiance is usually on the order of 3.10^{-4} W m^{-2} sr^{-1} μm^{-1}, allowing to resolve very subtle features in emission or absorption.

[18] Nightside and limb observations are used in this paper. In terms of spacecraft operations [*Titov et al.*, 2006], nightside observations usually correspond to science case 2 (off-pericenter disk observation, including movies), sometimes to science case 3 (observation from apocenter, including global mosaics); limb data are from either science case 2 or 7 (dedicated limb observations). Two different observing modes are used during operations: JHK mode (long exposure times to optimize signal-to-noise ratio at shorter wavelengths) and LM mode (short exposure times to avoid saturation at longer wavelengths). In JHK mode, only short-wavelength spectral channels are retained, to filter saturation; all such sessions are analyzed in the spectral range from 1.02 to 3.9 μm. For disk observations, pixels in the dark sky are filtered out; although they only contain Gaussian noise, the presence of outliers slightly affects the definition of the average disk component.

[19] The spectral cubes are calibrated in radiance (in W m^{-2} sr^{-1} μm^{-1}) using the latest version of the standard VIRTIS scheme, and saturated and unreliable pixels are set to zero. Multivariate analyses of this sort assume that spectra are directly comparable, and therefore that at least dark current and flat field corrections are of high quality. Conversely, they can shed light on calibration inaccuracies, and indeed the amount of details provided by the ICA has increased as the calibration scheme got more accurate. Spatial coefficients are here plotted as images (e.g., Figure 1b) or projected on geographic coordinates (e.g., Figure 3). In image view, the X axis corresponds to the spatial dimension of the detector while the Y direction is acquired through time. Small variations of the pixel to pixel response thus propagate through time and produce a vertical striation; defective pixels produce random patterns in vertical bands; localized events such as cosmic rays translate as points or short segments; flat field inaccuracies or temporal variations produce low-frequency variations in the horizontal direction. The same may apply in the spectral direction. The analysis is therefore restricted to the part of the detector which responds nominally, while columns producing systematic patterns are removed (for example, the first six columns are always removed). An additional difficulty is that spectral registration must also be uniform inside a cube (i.e., the channel-to-wavelength correspondence should be constant along the spatial direction of the detector), which is not always found to be the case at the nm level. This issue can only be approximately fixed by precise spectral resampling, which is not performed with the current calibration scheme.

[20] The ICA algorithm used here is the IDL implementation of JADE [*Moudden et al.*, 2005], with minor adaptations. A single additional constraint is applied to VIRTIS data in order to recover consistent signs of the components S and coefficients A from session to session. In general, both the spectral components and their spatial coefficients have positive and negative values. The normalizing convention applied here consists in forcing the spatial coefficients of each component to be positive in average. In particular, this convention results in positive features for the main contributions in the atmospheric windows, the O_2 emission band, and the upper layer thermal emission.

[21] Since most phenomena involved in this data set are multiplicative in nature, a straightforward idea is to analyze the logarithm of the signal. This potentially allows to separate a layer transmission from the emission of the underlying layers, and emissivity from temperature variations in a given layer. In practice however, this scheme does not provide satisfying results. The signal logarithm is dominated by random variations and instrumental patterns in the channels where the measured radiance is small, i.e., where the atmosphere is essentially opaque. Independent components derived this way are hardly usable, and have extremely noisy coefficient maps. More fundamentally, the objectives of the present study are not to derive fractions of the various components, but rather to evidence the modes of spectral variability and their spatial distributions. A more quantitative scope, such as deriving gas abundances or opacities, can only be reached through a radiative transfer approach. Such an approach cannot be applied to all spectra owing to long processing times, but a statistical analysis is

helpful in a first step to identify the diversity of situations, and possibly to select example spectra to be inverted. The approach adopted here is therefore to analyze the radiance directly, which still allows us to detect, e.g., variations of temperature with local time in a linear approximation.

[22] Owing to the rather demanding algorithm involved, JADE is applied in the spatial direction rather than the spectral one, and is limited to the first 10 components. This means that the images of all spectral channels are decomposed as mixtures of statistically independent images, while the mixing coefficients are spectra providing the actual components in the signal (i.e., equation (1) is transposed). Since only the first components of the whitened data are retained, the computation in both directions may not be exactly equivalent however. Comparisons have been performed on smaller VIRTIS cubes with ICA applied in the spectral direction, or in the image direction by retaining up to 30 components. In all cases, the differences proved to be small, and do not affect the interpretation.

[23] Studies based on ICA do not usually focus on component magnitudes, because of the scaling performed during the whitening phase. To interpret remote sensing data, it is however interesting to know the average contributions of the various spectral components to the measured signal. We use here the quadratic mean of the mixing coefficients to estimate these contributions. Since we are working in the spatial direction, this is done after proper scaling of the coefficient matrix so as to retrieve results similar to those of an ICA performed in the spectral direction (i.e., spectral components are first normalized to unit variance). Tests performed on controlled mixtures show that complete analyses in both directions are very similar, and that the contributions retrieved in these conditions are usually within ~15% of the actual mixing coefficients. These contributions are, therefore, representative of the percentage of radiance owing to each component in the spectral cube, but components are sorted by the ICA according to their inhomogeneity, which is usually related to the existence of clustering around several mean values. In this sense (which is different from variance analysis) the first components introduce more variability among spectra.

[24] In the following discussions, the physical meaning is derived from the spectral components themselves (normalized to unit variance) and the coefficient maps are used only to study the spatial distributions of the retrieved components. Other quantities used to interpret the results are the weighted components (normalized components × contributions, providing the spectral contributions in radiance) and the components' variability (normalized components × coefficients variance, used to estimate the spectral contrast).

3. Results

[25] This section presents extensive ICA results in several situations common in the VIRTIS data set: midlatitude observations with short integration time, adjusted to long-wavelength measurements; midlatitude observations with long integration time, stopping at 3.9 μm; observations of the south pole with long integration time. The main regularities encountered in these situations are outlined in this section.

[26] The VIRTIS data archive includes geometry files associated with each data file, which provide viewing angles and coordinates of each pixel on two reference surfaces: the Venus ellipsoid and an arbitrary cloud layer located at 60 km altitude. In addition, surface elevation is provided for each pixel as the average of the Magellan Global Topography Data Record (GTDR) [*Ford and Pettengill*, 1992] over the nominal FOV projected at the surface. This projection is performed along the geometrical line of sight neglecting refraction and scattering effects in the atmosphere. For limb observations, surface elevation is replaced by the tangent altitude, and all other quantities are computed at the tangent point. These quantities are computed with the Spice system, using navigation kernels provided by ESA. The nominal pointing accuracy is on the order of 0.01°, better than the IFOV size (see VIRTIS archive documentation [*Erard*, 2008] and associated documents). This information is used to draw maps of the data and to study variations related to viewing geometry (emergence angle and local time) and to surface elevation.

3.1. Midlatitude Views: Long Wavelengths

[27] A nine-cubes mosaic of the whole disk was acquired on orbit 67. The second of these cubes, analyzed here, is entirely composed of nightside data. It was acquired with short integration time (0.36 s, LM mode) therefore it is noisy at short wavelengths but does not saturate in the longer-wavelength channels. When applied to the complete spectral range, the ICA identifies three main components (Figure 1). All three components have spatial coefficients with average far from zero, and are always positive. Higher-order components are obviously dominated by instrumental effects (noisy lines, hot pixels, and stray light) or cosmic rays.

[28] The first component has a 58% contribution. It dominates the thermal signal (black body radiance, including absorptions by CO_2 -CO) and the shortest-wavelength emission peaks, and is a major contributor also in the midrange peaks at 1.74 and 2.3 μm. The coefficients have a spatial distribution which is rather uniform, displaying mostly low-frequency variations and only a subdued cloud pattern. The decrease toward the right of the image corresponds to the decrease in temperature to the west, as the atmosphere cools down with increasing local time in the night; this is by far the largest variability observed in the data. The long-wavelength end of the spectrum is fit by a 240 K black body, corresponding to an altitude of 59 km according to the VIRA profile; this appears to be the average altitude of the main thermal contribution to the spectra, i.e., the altitude where opacity equals 1 longward of 3 μm. The short-wavelength contribution to this component is the average radiance in the atmospheric windows.

[29] The second component has an overall contribution of 27%. It is mainly concentrated in the peaks, especially at 1.74 and 2.3 μm where this is the main contributor, and to a lesser extent in the black body. Its effect is to reduce the intensity of the black body, to add radiance in the CO_2 band wings, and to reduce the radiance in the atmospheric peaks. It therefore represents variations in the temperature of the emitting layer, plus variations in cloud opacity. The spatial coefficients have marked cloud structure at midlatitudes,

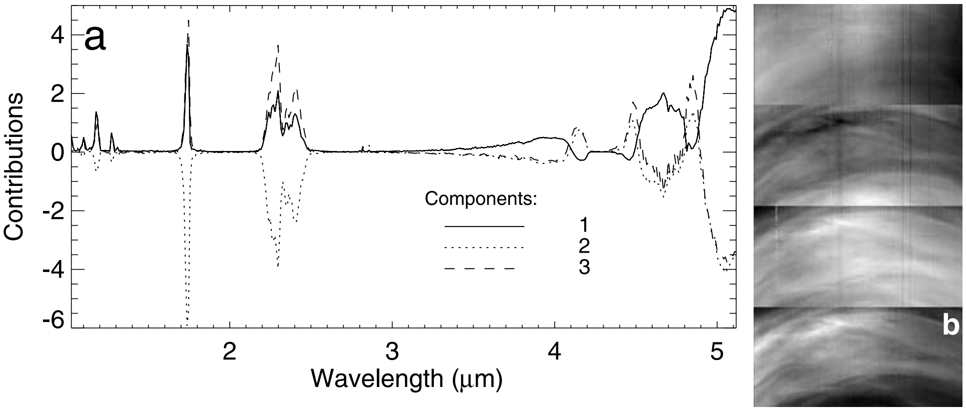

Figure 1. (a) Main three components for session 67_01 in LM mode, normalized to unit variance. The first component is the main contribution and responds to the blackbody and short-wavelength peaks. The other two components decrease the blackbody emission and either reduce or increase the short-wavelength peaks. (b) Spatial coefficients for these components in image format (west is on the right side). The bottom frame is the radiance measured at 1.74 μm plotted for comparison. In this case, all coefficients are positive.

related to opacity variations, and a maximum contribution at latitudes higher than 60°S, related to temperature.

[30] The third component has a 11% contribution. It is again related to the atmospheric peaks and to the wings of the CO_2 absorptions above 4 μm. Although the contributions are located at the same wavelengths as those of the second component, there is an opposite relationship between the long- and short-wavelength parts of the spectra: this component contributes essentially to increase the signal in the short-wavelength peaks, but also to remove intensity in the black body and to add radiance in the wing of the CO_2 bands. Spatially, it mostly displays an area located equatorward of 45°S where the 1.74 μm and 2.3 μm peaks have reduced intensity.

[31] Longward of 3 μm, components 2 and 3 are fit by black bodies at 230 and 220 K respectively. It is remarkable that the spectral components follow a Planckian function at long wavelengths, suggesting that they actually represent different temperatures although they are added to each other. It is likely that they represent spatial variations in temperature and altitude of the upper, emitting layer: the overall gradient in component 2 represents the cooling of the emitting layer with increasing latitude, but the variations in CO_2 band profiles qualitatively suggest an increase of altitude as well. This remains to be assessed by more quantitative radiative transfer. A part of the variability in the atmospheric windows is included in this component because it follows a similar latitudinal pattern, although it is related to opacity variations in a much deeper layer (lower to middle clouds). In contrast, component 3 is mostly responsive to the intensity in the peaks, and the black body contributes here mainly to remove the large-scale latitudinal pattern.

[32] As a conclusion, the various physical phenomena are not entirely separated in this situation: components 2 and 3 must be recombined to recover either the variations in the 1.74 μm peak or the latitudinal variations in the black body. Altogether, these two components define three areas: a midlatitude band dominated by warm black body and intense peak emission (or reduced cloud opacity); a high southern latitude area which has opposite properties; a lower-latitude area with warm black body and reduced peak intensity. These three areas are obviously related to zonal circulation. In addition, component 1 defines a cooler, deeper night region. Overall, the three components identified in this case do not appear related to different layers, but rather to the average signal and its variations with increasing local time (first component), or to latitudinal variations (next two components).

[33] ICA of the other night cubes of this mosaic reveal consistent patterns, with additional information at the limb (O_2 emission). In any case, the main contributors to the nightside signal appear to be the thermal black body, the peaks in the atmospheric windows (especially the 1.74 μm one and the 2.2–2.5 μm structure, representative of opacity in the lower and middle cloud layer), and the O_2 emission at 1.27 μm. Observations performed at short integration times are dominated by these variations. In the rest of this paper, only disk observations acquired with long integration times will be used, so as to evidence the more subtle signatures located at short wavelengths.

3.2. Midlatitudes: Short Wavelengths

[34] Successive global views of a given area ("movie" mode) were acquired on the nightside at reduced resolution during orbit 110. The area is centered at low to midlatitudes (15°N to −45°S) between Themis and Beta Regio (240°–275°longitude). Session 5 of this series is analyzed in this section. A long exposure time is used to optimize the signal-to-noise ratio at short wavelengths (JHK mode: summation of 4 frames acquired with an integration time of 3.3 s). Therefore, the long-wavelength channels are saturated, and the effective spectral range analyzed is in this case 1.02–3.9 μm, which includes just the onset of the thermal emission. The particularities observed in this session are (1) an extremely low opacity; (2) a large range of emergence angles, affecting both the thermal emission and peak intensities at 1.74 and 2.3 μm. These quantities appear to be strongly correlated at large scales, with a relatively sudden drop at latitude 20°S, as emergence reaches 60°.

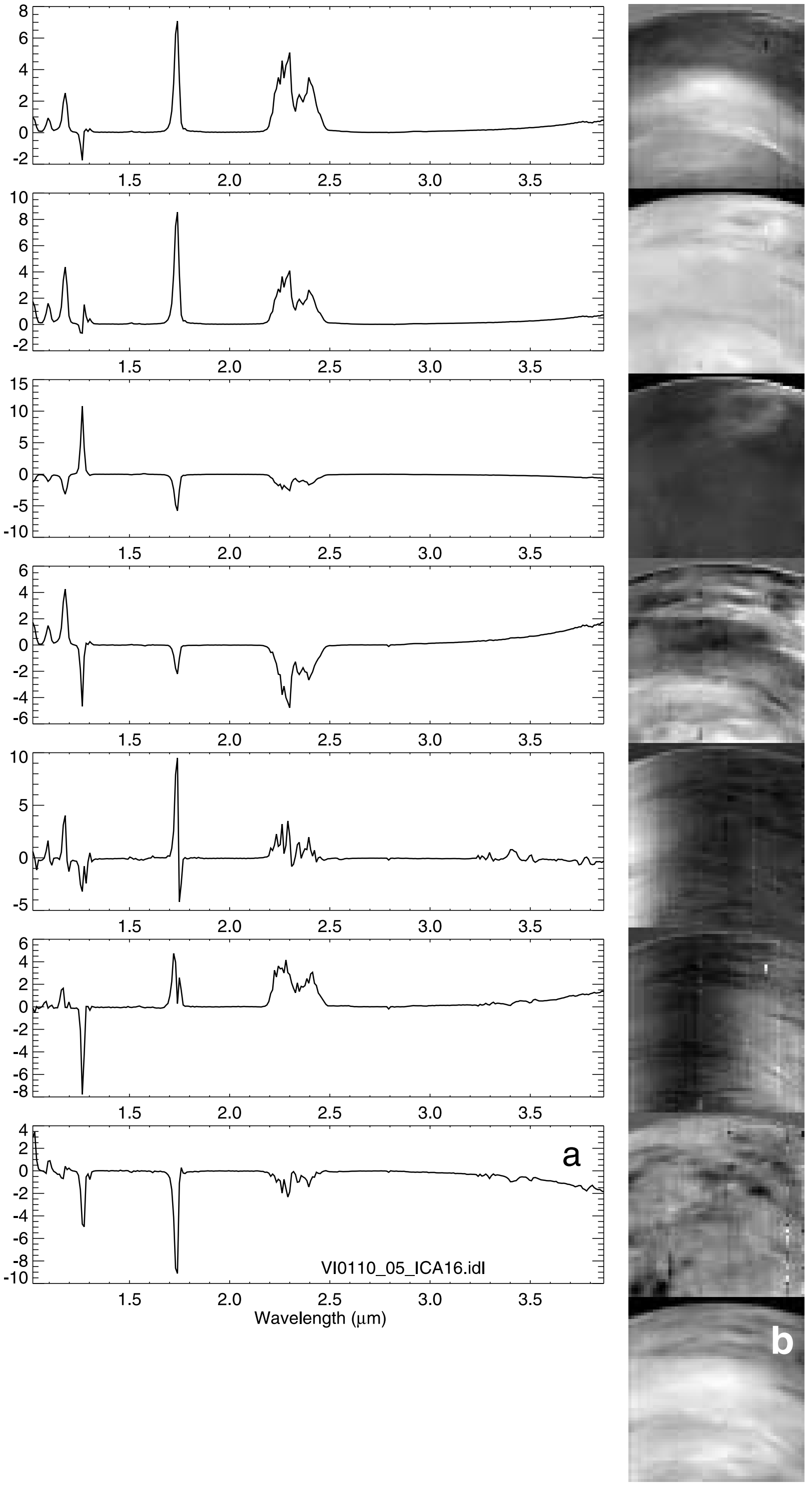

Figure 2. (a) Main components for session 110_05, acquired in JHK mode at middle to low latitudes, under low opacity. (b) Spatial coefficients for these components in image format (west is on the right side). The last frame is the radiance measured at 1.74 μm plotted for comparison.

[35] In this session the first 7 components have continuous spatial distributions (Figure 2). The second component has only large positive values, therefore it carries most of the signal and varies with the overall brightness but it only ranks second in terms of inhomogeneity introduced among the spectra. The third component (O_2 emission) also has positive values, and is therefore simply added in some locations. All other components are either positive or negative on the disk, with average and median values much closer to zero, and therefore represent modulations around the main component. These components represents more than 96% of the measured signal.

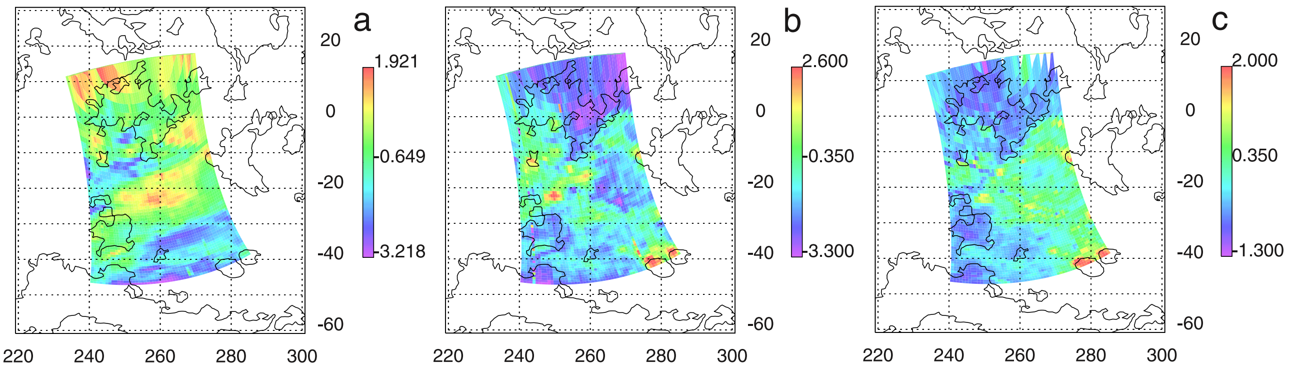

Figure 3. Session 110_05. Cylindrical maps of (a) component 4 (small-scale variability in the 2.3 μm structure, inverted), (b) component 7 (surface, inverted) compared to (c) Magellan topography integrated on the pixel areas (scale in km). The contours are from Magellan altimetry, contour interval is 500 m.

[36] The first component (10% contribution), in spite of its moderate contribution, carries most signal variability in the 2.2–2.5 μm structure, in the 1.74 μm peak, and in the black body emission. It has no contribution from the 1.28 μm peak, but is slightly opposed to the O_2 emission at 1.27 μm (i.e., it includes a negative contribution at this wavelength). This component depicts a strong variation with latitude: intense thermal emission and low cloud opacity observed at middle to high latitudes, while the reverse situation is found equatorward of 20°S. As mentioned above thermal emission and cloud opacity are correlated, although it is unclear if it is only an effect of viewing geometry (implying that the upper layer is not Lambertian), or if the temperature of the upper layer is decreased by the opacity of the underlying cloud layers. Another pattern in the component's distribution is an area centered at latitude 25°S which has maximum flux at 1.74 and 2.3 μm, and therefore minimum cloud opacity.

[37] The second component (60% contribution) is the main nightside signal, with large, positive coefficients on the whole disk, which dominates the radiance at all wavelengths except in the O_2 emission band. Although roughly similar to the first component, it includes a much larger (~50%) contribution in particular at short wavelengths, both in the atmospheric windows and between them. Interpeak radiance is mostly daylight signal scattered on the nightside, and is rather small in this session; it is only present in this component. This is also the only component which contributes significantly at 1.28 μm. Finally, this component includes faint but distinct structures at 1.31, 1.51, 1.55, and 1.78 μm. In spite of its dominant contribution to the signal, it carries only ~25% of the variability in the short-wavelength peaks, and even less in the 2.2–2.5 μm structure.

[38] The third component (19% contribution) carries the only significant contribution to the 1.27 μm peak and reflects the variability at this wavelength. Its contributions are negative in all peaks except at 1.27 μm. It stands for the O_2 emission from high altitude, which is especially marked at the limb and in a yin and yang shaped pattern at the top right of the image. This contribution is further discussed in section 3.3.

[39] The fourth component (3.5% contribution) has positive contributions from the first three peaks and includes the most intense thermal emission, opposed to the long-wavelength peaks at 1.27, 1.74, and 2.3 μm. Detailed examination of the data show that it is related to small-scale variations in the intensity of the 2.3 μm structure (Figure 3a). The black body contributes mainly to remove the large-scale variations between equatorial regions and higher latitudes, which are described by component 1. The resulting features have unusually small sizes (on the order of 100 km), and they are probably observed only because of the very low opacity in this session. They are tentatively interpreted as variations in the lower/middle cloud layer with either higher opacity, or different particle size.

[40] The fifth component (2.2% contribution) displays very unusual peak profiles in the atmospheric windows. In particular it detects a structure in the 1.27–1.29 μm peak (with different responses to the O_2 emission and to the aerosol window), but also in the 1.73–1.76 μm peak (opposing the two wings of the peak), inside the 2.2–2.5 μm structure and to a lesser extent in the 1.10 and 1.18 μm peaks. The spatial coefficients image is dominated by a strong gradient in the left part of the image. Coefficients are distributed around zero, therefore this component is either added or subtracted to the first ones. Altogether, this is the signature of a gradual shift of spectral registration along the spatial axis of the detector, which translates as a derivative effect in the sharp peaks and in the 2.3 μm structure.

[41] The sixth component (2% contribution) again exhibits unusual peak profiles, this time opposing a central minimum to maxima in the wings of the peaks. This is the typical signature of a second derivative effect (Laplacian), demonstrating that the spectral misregistration is not uniform along the detector. Spatially, it mostly affects the right part of the image. Both registration effects are small, less than 1 spectral step wide.

[42] The seventh component (1.5% contribution) is dominated by strong negative contributions from the 1.74 and 1.28 μm peaks, and positive contributions from the 1.02, 1.10, and 1.18 μm peaks. It is also opposed to the black body emission at long wavelengths. Comparison with the altimetry map demonstrates that this component includes a surface contribution, originating from the positive contributions in the short-wavelength peaks (Figures 3b and 3c). The comparison is particularly good in the southernmost region, where the emergence angle is minimum. Two

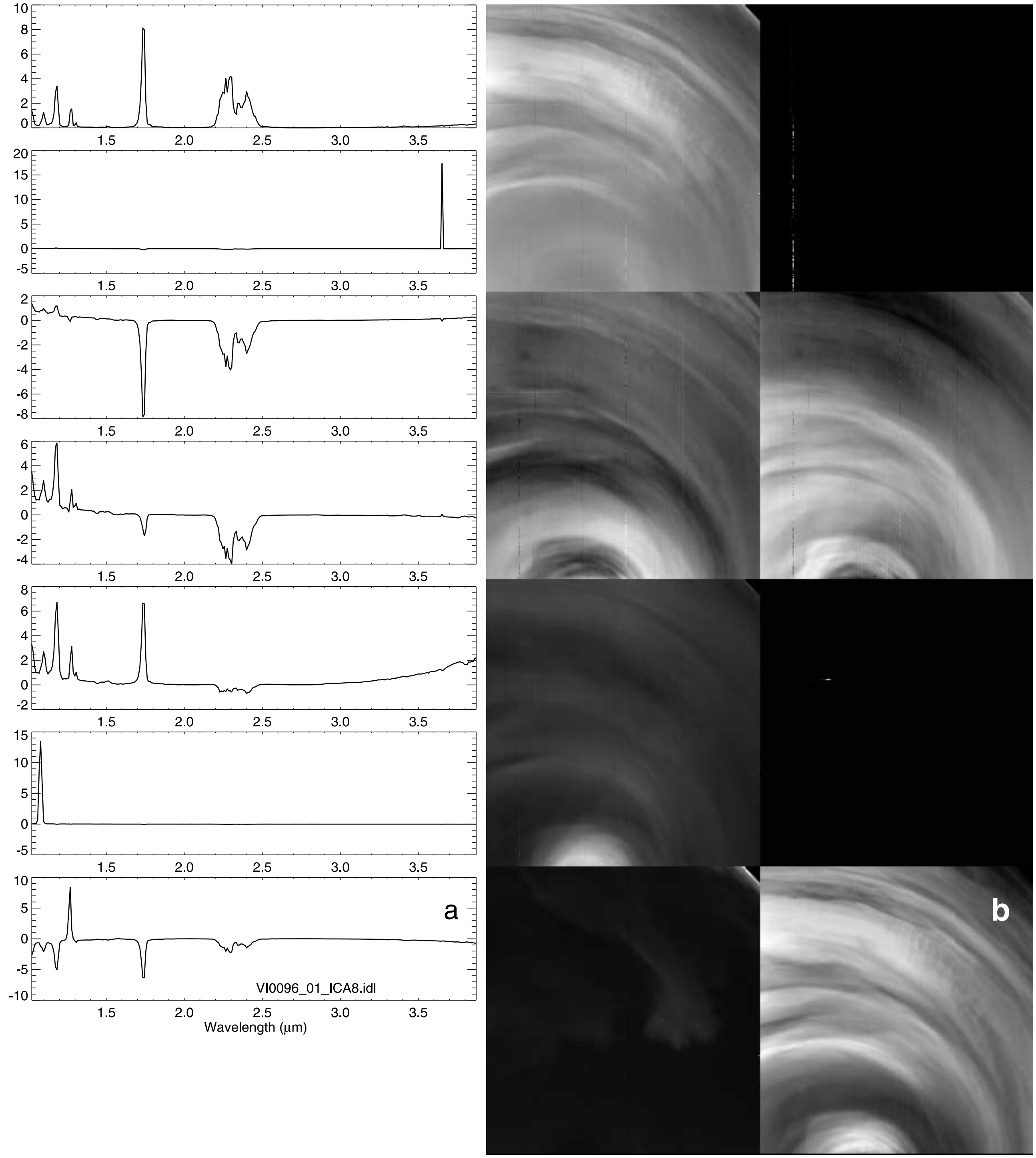

Figure 4. (a) Main components for session 96_01, acquired in JHK mode, acquired at high to low latitudes under large opacity and (b) spatial coefficients for these components in image format (west is on the right side). The last frame is the radiance measured at 1.74 μm plotted for comparison.

summits in Themis Regio (Shiwanokia and Shulamite Coronae) are identified without ambiguity, as well as smaller reliefs, although they are relatively modest in size (culminating at $\sim$2000 m over the datum). Depressions are also identified clearly, e.g., the one at 45°S, 245°E, which is 1600 m below the datum.

[43] The night sessions include much more details when acquired with longer integration times, owing to the higher signal-to-noise ratio available in the short-wavelength peaks. The components are in this case related to 3 different atmospheric structures, O_2 emission from high altitude, and a surface component. The three atmospheric components are: (1) the average atmospheric spectrum, varying with

normal brightness and controlled by the overall opacity; (2) the large-scale variations followed by all atmospheric windows and the black body emission, correlated with the emergence angle; (3) small-scale features mainly observed in the 2.3 μm structure. The latter two introduce small variations around the main contribution, but represent most of the signal variability. In addition, the O_2 contribution is extremely variable depending on the session, and can reach a 20% contribution. The very low and uniform opacity for this session highlights the variation of the signal with viewing geometry at all wavelengths, and allows to detect departures from this variation. Those are mainly observed at 1.02 and 1.10 μm, and at 1.74 and 2.3 μm. The former are identified as surface relief from their correlation with Magellan topography, the latter are tentatively interpreted as small heterogeneities in the lower cloud layer. The way various phenomena are detected and separated is based on differential detection, and is discussed in more details below (sections 4.3 and 4.4).

[44] Component 4 highlights small-scale structures about 100 km wide mostly related to the 2.3 μm peak intensity. This is reminiscent of holes observed in the lower/middle cloud layer, which are interpreted as localized evaporations [see *McGouldrick and Toon*, 2007]. There are two differences with these structures however: first, both positive and negative anomalies exist at this scale; second, these anomalies have much smaller size than the structures observed by NIMS on Galileo, for instance. Brighter structures in Figure 3a, which are larger in average, could correspond to holes in the cloud layer previously reported; the smaller dark spots in Figure 3a have larger opacity, and may be discrete clouds.

[45] The surface contribution is clearly detected in this session, mainly from its contribution to the 1.02 μm peak. As demonstrated here, elevation can be retrieved down to very low values, close to the minimum elevation on Venus, at least in situations of low opacity. This will be discussed further below. A last point worth noticing is that spectral misregistration, although detected with remarkable accuracy (including second-order effects) does not preclude the detection of lesser patterns in the data, because the various phenomena are efficiently decoupled by the ICA.

3.3. South Polar View

[46] Session 96_01 encompasses low to high latitudes from $-10°$ to $-80°$ around the 0h meridian, which is located at longitude 210°. Although it does not extend to the pole the session covers a part of the polar vortex, which is not centered at the pole. The range of emergence angles is even larger than on the previous example and the opacity is more typical of what is usually observed by VIRTIS, with a marked zonal cloud pattern. Five among the first seven components have continuous spatial distributions (Figure 4).

[47] The first component (44% contribution) dominates all the atmospheric peaks, including the secondary ones at 1.31 and 1.51 μm. It is interpreted as previously as the main Venus signal, with modulation by the lower and middle clouds. In contrast to the previous session though, it has only a limited contribution in the thermal range ($\sim$30% above 3 μm). This difference is partly due to the larger opacity variations but mostly to the presence of the warm polar area, which decouples the peaks from the black body. Although the component is controlled by the 1.74 and 2.3 μm peaks, the very prominent cloud pattern observed in the polar region at these wavelengths is much attenuated. It is preserved only at midlatitudes (equatorward of 50°S) where the intensity of the two peaks varies in proportion. Apart from these variations, the component is globally correlated with the emergence angle, like short-wavelength peaks are, and to a lesser extent with local time.

[48] The second component (9% contribution) is related to a pair of hot pixels which behave erratically in this session. This information is entirely separated from the actual signal from Venus.

[49] The third component (14% contribution) is dominated by the 1.74 and 2.3 μm peaks only, with no thermal contribution. Since it has positive coefficients with a negative spectrum, it represents a decrease of radiance in these peaks (large values correspond to large opacity). The component is mainly related to varying relative contributions in the two peaks, while the short-wavelength contribution compensates the large-scale dependence with emergence and local time. The spatial distribution mostly opposes a polar collar (with maximum values) to both the vortex and a middle to high latitudes zone (55°S to 70°S), but it also evidences a fine-scale concentric structure inside the polar vortex. This pattern is essentially present in the distribution of the 1.74 μm radiance, therefore this component is certainly responsive to varying cloud opacity at high latitudes, perhaps amplified by photometric effects or a different size distribution.

[50] The fourth component (9% contribution) has a strong signature at short wavelengths, in opposition to the long-wavelength peaks, and no thermal contribution. The spatial pattern is rather complicated: it mainly opposes middle and high latitudes ($\geq$50°S) to a zone of minimum values from 30°S to 40°S, but also two concentric areas in the vortex itself (delimited at 78°S). Besides, it evidences a nonzonal opposition in the external area of the vortex and the polar collar; this latter pattern is congruent with a similar distribution of component 5, with a subtle boundary located at $\sim$195°longitude, running from the pole to 50°S. It suggests the presence of a high-altitude haze in the polar areas, although it is only present in the 1.74 μm peak. The concentric pattern observed in the polar vortex is not present in maps of the 1.74 and 2.3 μm radiance, and appears to result from different variations at these two wavelengths. According to *Carlson et al.* [1993], radiances at 1.74 and 2.3 μm vary with the emergence angle and their ratio increases with larger particle size [see also *Wilson et al.*, 2008]. The photometric effects are expected to be very small in the polar areas, owing to the narrow range of emergence, so that the variability in this component is mainly related to particle size variations: the outer vortex area appears to be dominated by larger particles, while smaller ones are found in average in the inner region; but both areas are made of interleaved rings with changing particle size. A similar opposition occurs at lower latitudes, on much larger scales.

[51] The fifth component (11% contribution) is like the first one essentially positive, but has near-zero contribution from the 2.3 μm structure, significant signal at short wavelengths, and the only noticeable thermal contribution (this is the main contributor longward of 2.9 μm). It is therefore controlled by the temperature of the upper layer. Short-

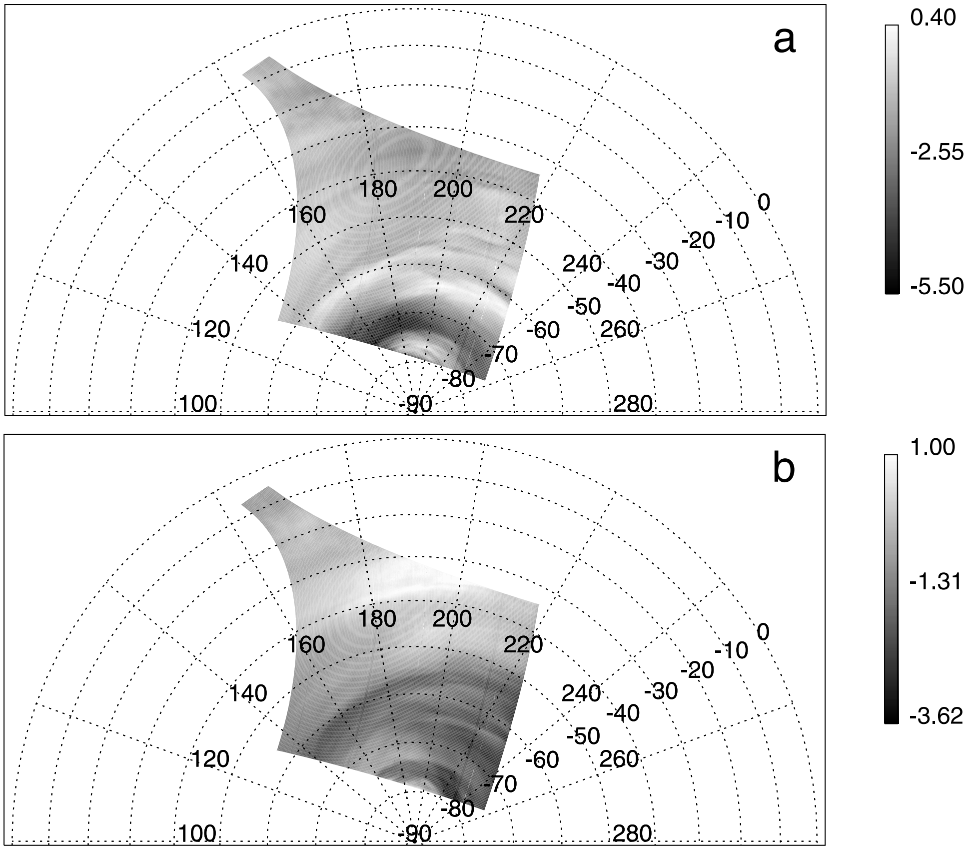

Figure 5. Maps of components (a) 3 and (b) 4 in session 96_01, evidencing the concentric structure in the polar region.

wavelength peaks are associated with it because they reach maximum values on the vortex, suggesting a different size distribution. They also appears to be affected by especially intense limb darkening, which is centered at the pole in this view. Spatially, the component opposes the vortex area to the rest of the scene, with a border located at about −75°S. This component also includes a feature observed only at long wavelengths: tenuous, narrow features suggesting high-altitude, warm clouds ranging down to 55°S.

[52] The sixth component (3.9% contribution) describes a severe cosmic ray event on the matrix, extending in the spectral and spatial dimensions but limited to a single time step (3 spectral channels wide, extending on ~20 pixels).

[53] The seventh component (4.8% contribution) is dominated by the short-wavelength side of the 1.27 μm peak, in opposition to the other atmospheric windows. It represents the O_2 airglow, with a very strong limb signal and a characteristic nonzonal, high-altitude cloud pattern entirely decoupled from the other components.

[54] This example differs from the previous one by higher opacity and larger extension toward the south pole. The analysis results in five main components all related to the atmosphere: the bulk signal and its main variations (component 1); two components related to additional opacity variations (components 3 and 4, see Figure 5); a high-altitude component related to polar temperatures and limb darkening (component 5); the O_2 emission, as usual completely independent and easily separated (component 7). Not unexpectedly, the large opacity precludes the observation of surface features (see Figure 6 and section 4.5).

[55] Photometric dependence is expected to be different in each atmospheric window depending on opacity [see *Grinspoon et al.*, 1993], so that the relationship between the peaks is a function of emergence angle. In this session with large opacity variations, the variations at large emergence are included in components 1 and 5, while opacity variations under low emergence define another component 3. Besides, a changing size distribution also affects the photometric behavior, and is included here in components 4 and 5 (the latter mostly driven by temperature variations of the upper layer in the polar area). Similar secondary photometric variations in the northern polar region have been interpreted by *Carlson et al.* [1993] as related to the ratio of mode 2′ and mode 3 particles in the clouds. The map of component 4 (Figure 5b) is actually similar to their image of branching parameter in the northern hemisphere. Such a variation can result either from varying particle densities in individual layers, or from changing layers thickness.

[56] The general pattern observed in most sessions covering the vortex typically defines five main areas:

[57] 1. A middle- to low-latitude zone (50°S to 10°S) which usually displays whirling patterns of middle to lower clouds and includes mottled structures due to gravity waves. The southern limit roughly corresponds to a sharp transition in zonal velocity [*Sanchez-Lavega et al.*, 2008].

[58] 2. A high-latitude zone (70°S to 50°S) with more regular flow.

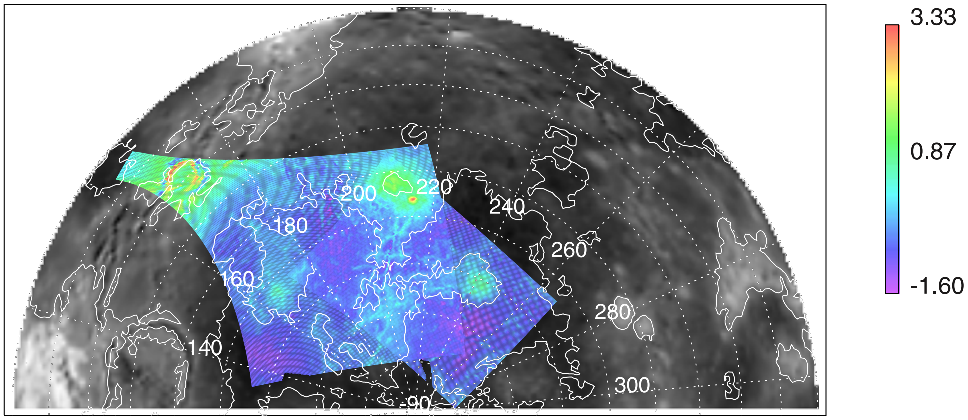

Figure 6. Magellan topography for sessions 96_01 and 112_01. The background map is a low-resolution version outside the area of interest. The scale is in km.

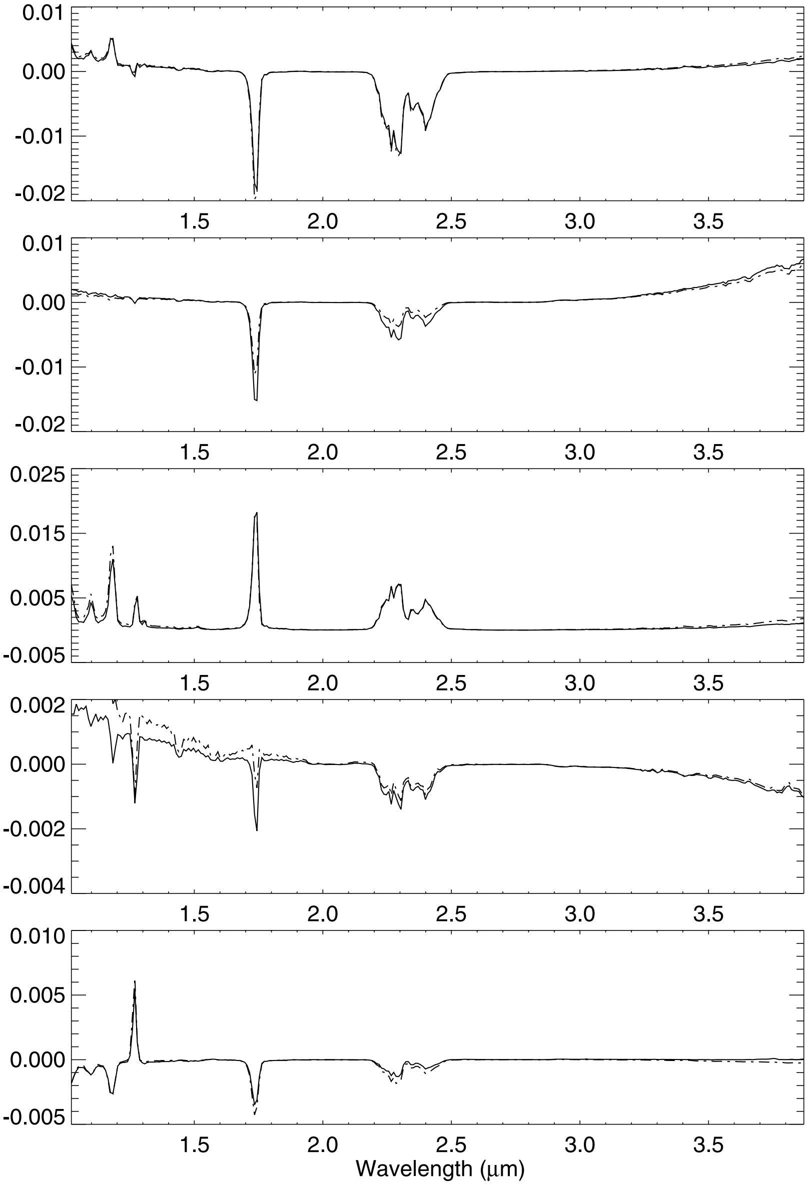

Figure 7. Matching spectral components in sessions 84_01 and 84_03, two parts of a movie covering approximatively the same area. Apart from the fourth one which concentrates a small, changing, dayside contamination, these spectral signatures are very similar between the two sessions.

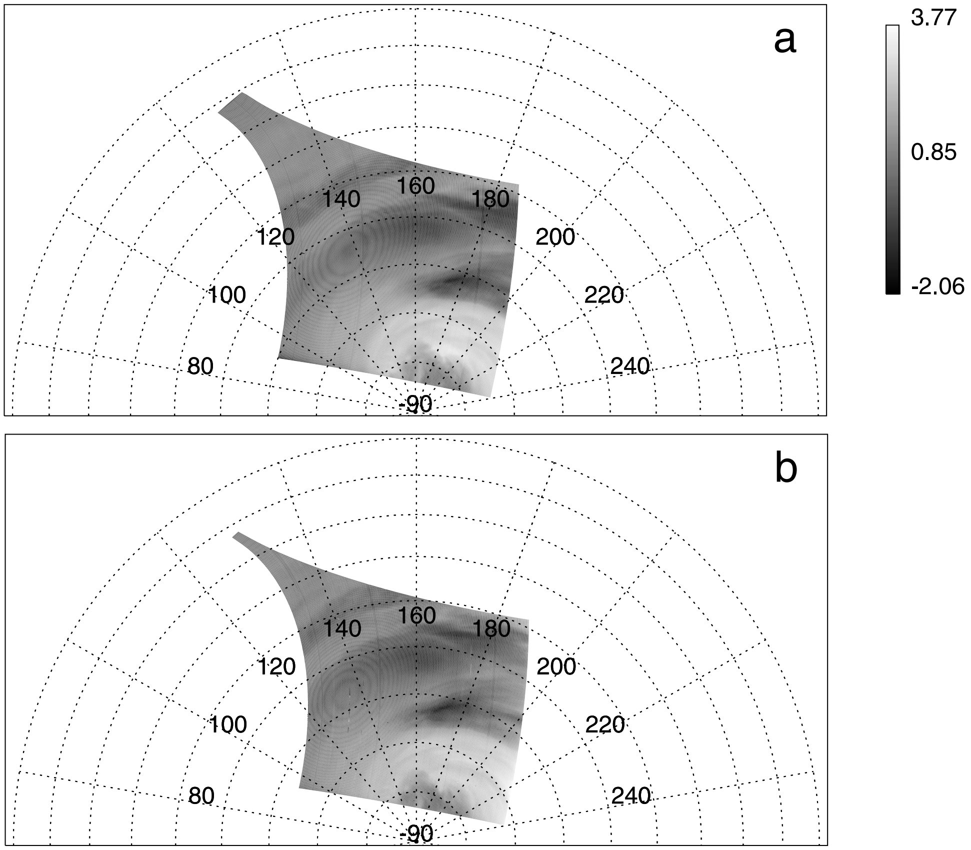

Figure 8. Maps of component 1 in (a) session 84_01 and (b) session 84_03. The same components are retrieved by ICA, although in a different order. Paired components such as those have nearly identical spatial distributions, demonstrating that the method is extremely robust to noise, random events, and small variations in the signal.

[59] 3. The polar collar (74°S to 70°S) here delimited on components 3 and 4.

[60] 4. The polar vortex (74°S), globally warmer, which appears composed of an external and an internal areas separated at latitude ~78°. The contrast is related to the average particle size, with larger particles in the outer vortex. All the vortex is made of many concentric rings with contrasted opacity. This concentric pattern at high latitudes is illustrated by the polar maps of components 3 and 4 in Figure 5.

4. Discussion

4.1. Robustness and Consistency

[61] The comparison of successive cubes of the same movie demonstrates a very strong stability of the signal decomposition relative to noise, random events such as cosmic rays, and small variations of signal contents. This is illustrated by ICA of sessions 84_01 and 84_03 on the south polar area, which have been acquired 80 min apart and cover slightly different areas. Five of the first six components are related to the main atmospheric signatures (Figure 7): the lower/middle cloud signature bearing most of the variability (component 1, inverted on the plots); the warm and strong scattering spectrum typical of the vortex (component 2); the middle/upper clouds component which always dominates the signal (component 3); the O_2 emission component (component 2); a specific day side spectrum which is observed in all sessions approaching the terminator, and apparently also includes the particle size variations.

[62] Although paired components represent nearly the same fraction of the signal in both sessions, they do not appear in the same order because their histograms are slightly different, and because random events can produce intermediate components. Components describing the same information in two such sessions can be paired by looking for the best correlations between the two sets of components, and rejecting those which do not have an expression in both sessions. The maps of paired components usually compare very well. Figure 8 shows the maps of the first component in sessions 84_01 and 84_03, plotted with the same scale. The same cloud structures are present and easily identified, with little deformation at this time scale. Other components have equally similar maps, including the O_2 emission which varies at a time scale of some hours.

[63] In this typical example, cosmic rays and random signal from hot pixels vary noticeably between the two sessions, and produce some of the major components in only one session. However, the main physical components are still identified and their signatures are preserved (see also components 2 and 6 in session 96_01 above, Figure 4b). Of particular interest is the robustness of the analysis to changing information content. In this case, a larger portion

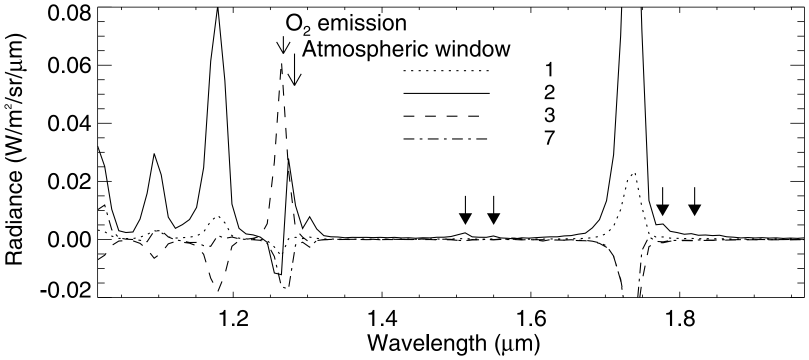

Figure 9. Four selected components from session 110_05 at short wavelengths. The first three are from the atmosphere. Component 7 carries the surface signal and is multiplied by 10 for clarity. This plot illustrates the separation of the 1.27 and 1.28 μm channels (components 3 and 2) and the differential detection performed by the algorithm. The scale in radiance provides the actual contributions of the components. Solid arrows indicate secondary atmospheric windows which are associated to the main signal in all sessions.

of the observed area is contaminated by day side signal in the first session, which modifies the spectrum of this component (it contains larger scattering and absorption signatures). In spite of this, the other spectral components remain unaffected.

[64] Another, more critical assessment of robustness consists in comparing several analyses of the same cube, with different type of filtering applied. At this level of calibration, several defective pixels and clusters are present and left uncalibrated in the cubes (either saturated pixels set to 0, or hot pixels with occasional abnormal output level). We compare here analyses of these cubes in their complete form, and after removal of the columns presenting the largest problems. A first situation is encountered when hot pixels affect spectral channels lying outside the atmospheric windows: in this case their are described by a specific component, and removing these columns do not change the definition of the other components. The second situation occurs when dead pixels affect channels inside the atmospheric windows, which takes place at least in two instances: a cluster affecting 3 columns and 2 channels located at 1.10 μm; another cluster affecting 2 columns and 2 channels located at 1.19 μm. Both fall in the short-wavelength peaks, which include atmospheric and surface contributions. When these pixels are preserved and set to 0, components which are defined mainly through a specific spectral shape in the corresponding range (surface contributions in both cases) have coefficients 0 in these columns; other components which include a minor contribution from these channels have slightly different values in these columns. The main result is therefore that components defined by the dead pixels include a part of the information relevant to the short-wavelengths peaks, which is especially sensitive when the surface signal is very apparent (e.g., session 411_02 analyzed below). In this case, the surface signatures are diluted in several components, some of which are driven by instrumental effects. In such situations at least, filtering of the affected columns is clearly preferred to simplify the analysis and its interpretation.

[65] When dead pixels are filtered, the overall results improve but are not entirely different. Components dominated by other spectral ranges (e.g., cloud opacity or thermal emission) are almost unchanged spectrally and have the same coefficient maps, as well as the same contribution to the signal. Components dominated by the short-wavelength peaks may be merged, and this information is then more readable. In session 411_02, three of the first ten components appear to include a strong surface signal when dead pixels are present, whereas the last two are combined when dead pixels are filtered, and represent about the same contribution to the signal. These contributions will be analyzed below, but the important point here is that the current method appears extremely robust to the addition of spectrally localized artifact, even when they affect essential spectral signatures: in the worst case, only the affected signatures are split among several components but they are still identifiable and the other ones are unchanged.

4.2. Minor Atmospheric Windows

[66] The component which carries the main contribution to the signal always corresponds to the emission of the lower atmosphere modulated by the cloud opacity. It therefore includes peaks in the main atmospheric windows, and sometimes a weak contribution from scattered daylight at short wavelengths. Other, subdued features appear to be systematically present in the spectrum of this component. Three such features are of particular interest: two small features centered at 1.51 and 1.55 μm, and a wide feature ranging from the 1.74 μm peak up to 1.86 μum, with secondary maxima located at 1.78 and 1.82 μm (Figures 9 and 10). The 1.51 μm feature and the 1.78 μm maximum have intensity ranging from 20 to 30% that of the 1.31 μm window, and the 1.55 and 1.82 μm features are another factor of 3 fainter in general. The widest of these signatures is the 1.51 μm one, which is detected on two spectral channels, and is on the order of 20 nm wide (FWHM).

[67] These features are not systematic artifacts, and they are not observed in the flat field nor in the calibration data. They are always associated to the main component, even when scattered daylight is large enough to define a specific component (e.g., component 4 of session 84_01, Figure 7). The intensity images in these channels, although very noisy, are correlated to those of the main atmospheric windows,

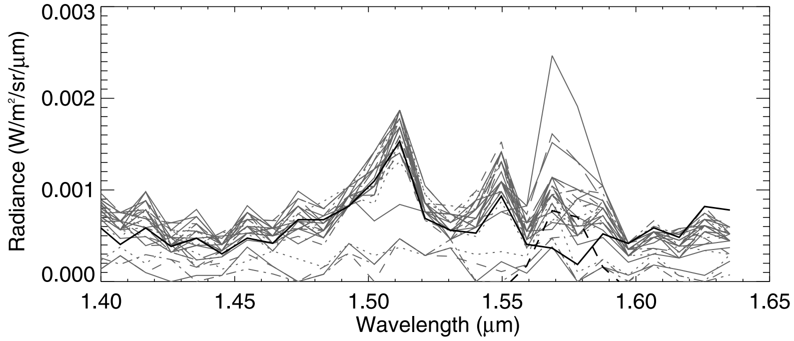

Figure 10. Individual spectra in session 110_05, sampled from the dark sky to the disk across the limb. The average noise is about 150 μW m^{-2} sr^{-1} μm^{-1} in each channel. The 1.51 and 1.55 μm features are very faint atmospheric windows which have the same spatial distribution as the 1.74 μm peak. These features are detected on component 1 (solid line). The 1.58 μm O_2 emission feature is unambiguously detected at the limb and stands above the noise without summation in this case. The feature is detected on component 3 (dashed line).

and do not increase toward the terminator, like scattered daylight does. This behavior is different from a probable artifact which is easily identified at 1.44 μum: this latter feature is present on several components, and is particularly marked in the one representing scattered daylight. The 1.44 μm location also corresponds to the border of a filter in the M-IR optical path, and is therefore expected to be affected by spurious effects in some situations. Finally, similar peaks are present at 1.51 and 1.52 μm in a theoretical spectrum published by *Kamp et al.* [1988], although these small features are not discussed in this paper.

[68] We therefore interpret the features at 1.51, 1.55, and 1.77–1.86 μm as minor atmospheric windows, where cloud opacity is not large enough to block the radiation from the underlying layers completely. Their intensity is very small and they hardly stand above the noise in VIRTIS measurements (Figure 10), which explains why they have not been reported from previous observations. Owing to the dissymmetry of the 1.74 μm peak, the secondary maximum at 1.78 μm could be related to an absorption on the shoulder of the peak; such absorption is expected, e.g., from H_2O. Although their intensity is very small, these windows may prove to be useful to study atmospheric composition in a specific range of altitude.

4.3. O_2 Airglow

[69] Recombined O_2 is detected through its main emission at 1.27 μm, partly overlapping the 1.28 μm atmospheric window at VIRTIS resolution [*Gérard et al.*, 2008]. The specific O_2 component has therefore its main positive contribution from this channel. The O_2 emission is concentrated in some areas where is dominates the signal in this channel. In other regions the lower cloud pattern is visible at this wavelength, and is extremely similar to the one measured at 1.74 and 2.3 μm, which is incorporated in another component. In order to optimize the independence of the components, the algorithm subtracts a part of the flux measured in the atmospheric windows to remove the cloud pattern from the O_2 component. Conversely, a part of the flux at 1.27 μm is subtracted from the main cloud components (Figure 9). The resulting O_2 maps are usually decoupled from other components even when the underlying vortex and cloud pattern is very strong (e.g., Figure 4a). The 1.27 μm band of O_2 is almost always observed on nightside sessions, except in rare occurrences (e.g., session 112_00).

[70] Another, much fainter signature of O_2 is located at 1.58 μm, and is detected by VIRTIS in some instances [*Piccioni et al.*, 2008]. In session 110_05 analyzed above, component 2 is responsive to O_2 emission. This component is the only one which has a larger relative weight than component 3 in a part of the spectral range. Interestingly, this occurs not only at 1.27 μm, but also at 1.58 μm in the fainter O_2 band. Indeed, a very marginal maximum is detected around the limb at this wavelength. Examination of the individual spectra however clearly evidence this feature without summation, at a level which is at most 10 times the noise (Figure 10). The ratio of integrated bands measured on this component is 102?20, to be compared with a value of 78?8 measured in better conditions at the limb in orbit 317 by *Piccioni et al.* [2008]. The spectral component is therefore representative of an actual emission spectrum. What is remarkable here is the ability of ICA to identify and locate an extremely small signature which is present in less than 1% of the spectra. More usual variance analysis methods would not extract such marginal features from the noise.

4.4. Surface

[71] A surprising characteristic of the data set is that the surface signature is clearly observed in many sessions, at least in a part of the observed areas. This signature stands out readily with ICA. The identification is unambiguous because, although based on spectral interpretation, it can also be checked by comparison of the coefficient maps with the GTDR. The strength of this surface contribution is due to VIRTIS improvements in terms of spatial resolution and signal to noise with respect to previous observations.

[72] Specific study of surface elevation from VIRTIS data [*Mueller et al.*, 2008] is based on the short-wavelength peaks intensity, mostly at 1.02 μm. It includes subtraction of scattered light measured between the short-wavelength peaks, correction of limb darkening in these peaks, and removal of the cloud pattern. The limb darkening rate is the

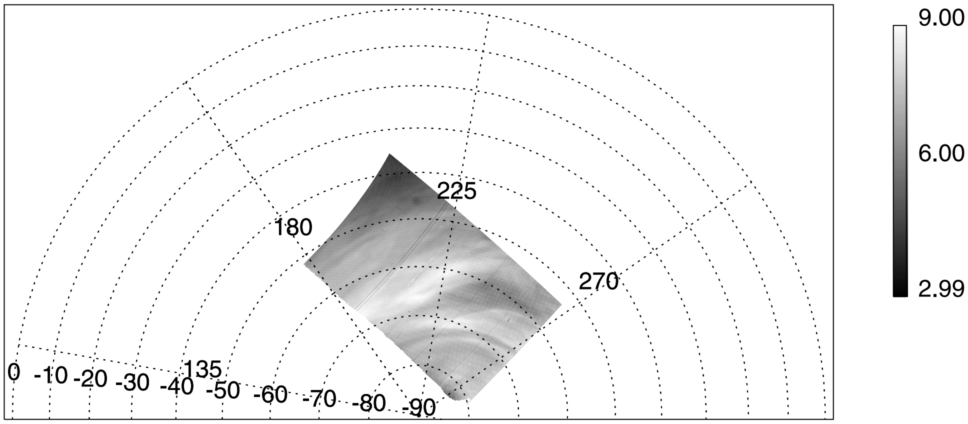

Figure 11. Component 2 in session 112_0, the main atmospheric signal. Idunn Mons is visible as a circular spot with lower intensity at ∼215°E, 45°S.

variation with emergence fit on the data; cloud pattern removal is performed through division by the radiance measured in a channel where the surface contribution is negligible, and accounts for multiple reflections between the surface and the atmosphere (following a two-stream model by *Hashimoto and Sugita* [2003]). This process involves assumptions of atmospheric temperature, cloud reflectivity, and surface emissivity, which have to be adjusted on the basis of the data.

[73] The ICA performs similar corrections, although because ICA is a linear analysis, they are only based on differences of radiance at various wavelengths. As expected, the surface is only detected through the short-wavelength peaks, which have the only positive contributions. The interpeak radiance is subtracted to remove scattered light, a large-scale limb darkening correction is performed through removal of the black body emission, and radiance in the long-wavelength atmospheric windows is subtracted to minimize the remaining cloud pattern. An enlargement at short wavelengths is provided in Figure 9 for session 110_05 (component 7). The derivative effect seen in the short-wavelength peaks corresponds to a larger surface contribution from the long-wavelength side of the peaks (according to *Meadows and Crisp* [1996]). The ICA detection is expected to be more robust than estimates based on a single peak intensity, because it takes advantage of all the surface-related information in the spectra. The result is however not directly given in terms of black body irradiance; it is a weighted average of all contributing wavelengths, and is therefore not easily translated as a surface temperature.

[74] In the data files analyzed so far, three situations may occur: (1) no surface component identified; this is usually related to short integration times (low signal-to-noise ratio in the short-wavelength peaks) and high opacity, (2) limited detection, usually in situations of high opacity (translating in intense short-wavelength peaks), or (3) complete detection, in sessions with low opacity. In the latter case, even the main atmospheric components may actually include a surface contribution identified in the coefficient maps.

[75] Examples of high opacity situations include sessions 96_01 (discussed in section 3.3), 112_0, and 84 (discussed in section 4.1).

[76] Session 96_01 encompasses an area with little marked topography, except for Atahensik Corona in Aphrodite Terra (170°E, 20°S) which is observed under extremely large air mass, and an isolated plateau (Imdr Regio) which culminates with Idunn Moons at more than 3000 m (215°E, 45°S). The rest of the area is made of low plains with subdued topography, ranging from –1600 to 0 m. As mentioned in section 3.3, the atmospheric components include intense scattering at short wavelengths. However, careful examination of components 1 (the lower to middle clouds comprising the bulk of the signal), 3, 4, and 5 (main atmospheric variations) shows a circular spot of low values over Idunn Mons (Figures 5a and 5b, and comparison with Figure 6). On component 1, the large elevation contrast in the Atahensik Corona area is also barely detected under large emergence. Session 112_00 is another polar observation with a large overlap on the previous one, in particular over Idunn Mons. Again, the summit is clearly identified as a circular feature on the main middle to high clouds component (Figure 11). Other possible surface detections may exist in these sessions but are marginal or not entirely convincing.

[77] In both cases an indirect detection is performed, the highest relief being detected as a local minimum of radiance in the main atmospheric signature. This is surprising. In both sessions, the feature is present in the 3 peaks at 1.02, 1.10, and 1.18 μm. The main atmospheric component is particularly responsive to the 1.18 μm peak and exhibits more contrast than direct measurements. The detection is thus not related to a particular spectral signature, but to the thermal flux from the surface: the presence of a topographic high results in missing signal from the strongly scattering layers located at much higher altitude. The surface therefore always contributes significantly to the outgoing flux, and colder local boundary conditions at the bottom of the atmosphere over higher areas translate as local minima of the outgoing flux. Consequently, low areas surrounding Idunn Mons are expected to be visible, and even more contrasted because of their higher temperature, but these variations are not observed.

[78] Because Idunn Mons is detected with its apparent size unaffected by blurring processes, we can conclude that blurring by cloud layers only affect spatial scales smaller

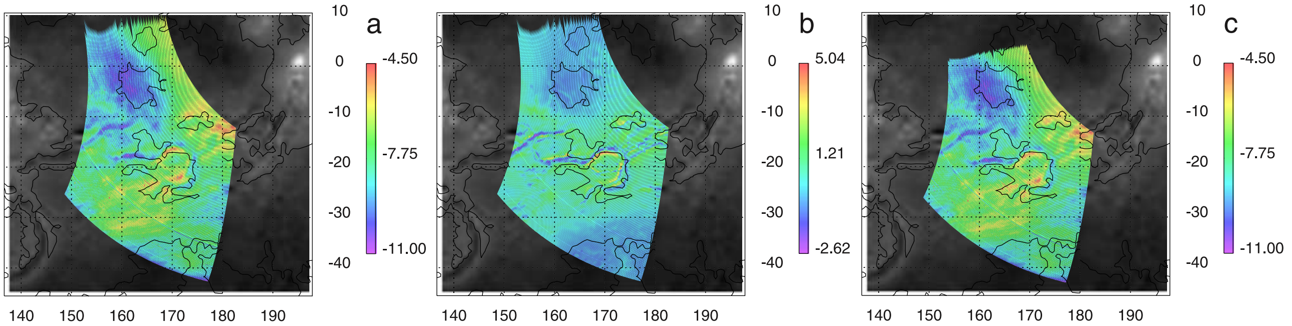

Figure 12. Cylindrical projection of component 9 (surface related) from session 411_02: (a) projection on the ellipsoid, (b) comparison with Magellan altimetry at the same resolution, and (c) projection of the data on the upper cloud layer at 60 km altitude. Atahensik Corona appears slightly displaced on Figure 12a, which is ascribed to refraction effects, while the correlation is much better for Figure 12c. The background image and contours are the low-resolution topography from Magellan.

than this (~100 km). This blurring scale is not expected to vary greatly with surface elevation, which is small compared to the altitude of the cloud layers. In order to mask the contrast in low-elevation areas, blurring should take place below the summit of Idunn Mons, which implies the presence of a high opacity layer near the surface in some occasions. This is reminiscent of reanalysis of Venera 13/14 descent measurements which indicates a layer of increased extinction at altitude ~1.5 km above the surface, in low-plain areas [*Grieger et al.*, 2004].

[79] Similar observations are performed on several occasions in the Idunn Mons area, while larger elevation contrasts are discernible over Aphrodite Terra in the same sessions (e.g., Atahensik Corona in session 96_01, Arthemis in session 84_03). This suggests that the inferred scattering layer is occasionally present only on topographic lows of the southern hemisphere, but not on highlands at lower latitude. Since low reliefs areas are observed in some instances (e.g., session 110_05, Figure 3a) this blurring is unlikely to result from CO_2 absorption or Rayleigh scattering at the bottom of the atmosphere, which are related to pressure and are not expected to vary greatly with time. Aerosols present at high altitude are not stable at such pressures, therefore the inferred scattering is most likely related to uplifted dust in the first kilometer above the surface. Another possibility is related to the condensation of volatile metals at the bottom of the atmosphere [*Schaefer and Fegley*, 2004]: in particular, condensation of Pb or Bi sulfides at 2.6 km altitude have been considered consistent with Venus geochemistry, and could form a scattering layer above the low plains.

[80] The surface is more visible when scattered daylight is reduced, i.e., when most components are flat at short wavelengths. This is the case for session 110_05 discussed above, but also for a set of sessions acquired during orbits 410 and 411 far from nadir viewing, when the atmosphere was particularly transparent. These sessions encompass the region around Atahensik Corona and Rusalka Planitia, including the Vega 2 landing site. The components are similar to those retrieved for session 110_05, with a specific surface detection in component 9 mostly responsive to the flux at 1.02 μm. The strong similitude of the coefficient map with Magellan altimetry confirms the surface origin of this component (Figure 12). In particular, the very specific surface features around Atahensik Corona are clearly identifiable.

[81] Comparisons between the GTDR surface features and those observed by VIRTIS allow to assess atmospheric

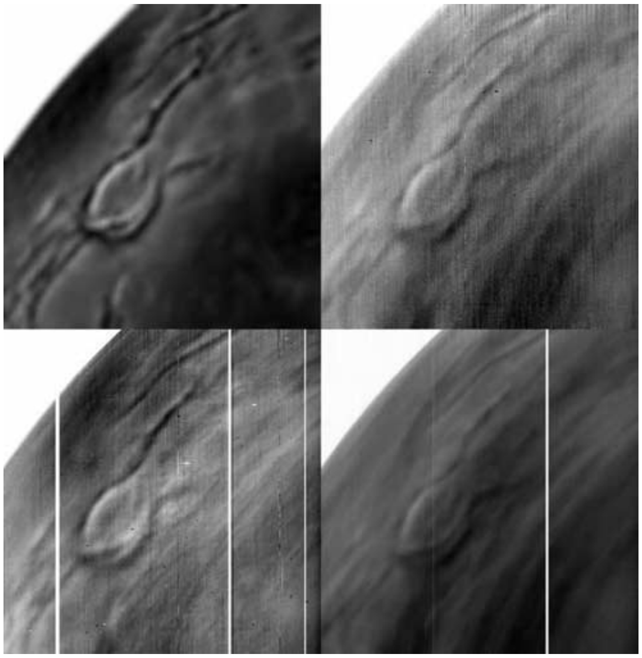

Figure 13. Surface-related information in session 411_02. (top left) Magellan Global Topography Data Record averaged on pixels surface (then box averaged on 6 pixels); (top right) measured radiance at 1.03 μm (inverted); (bottom right) measured radiance at 1.185 μm (inverted); (bottom left) component 9, inverted (filtered clusters appear as white columns). Although the main surface features are clearly identified in the radiance images, they are mixed with marked, unrelated cloud patterns. The surface component retrieved by the ICA is a simple linear combination of channels which minimizes these patterns and improves the contrast in some areas (e.g., bottom right corner).

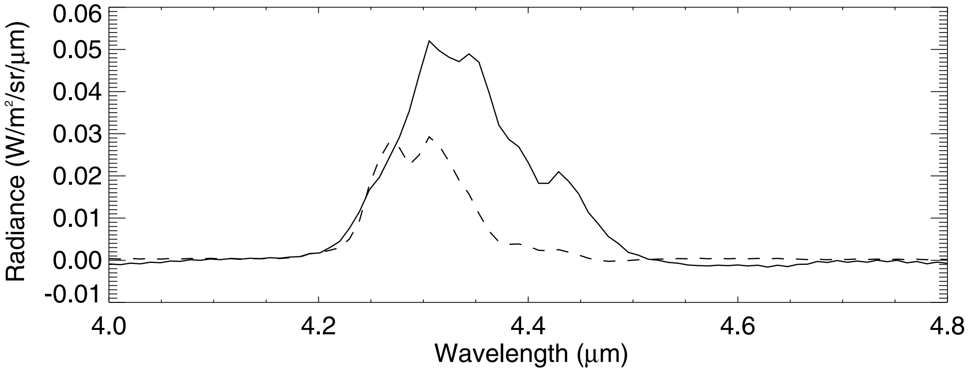

Figure 14. Components 8 (solid line) and 10 (dashed line) in tangential limb session 43_00, which are related to different regimes of CO_2 fluorescence in the upper atmosphere.

scattering effects. Session 411_02 is particularly adapted to this purpose, because of the low opacity and large emergence angles. The good fit at the limb between signal cutoff and emergence computed on the upper cloud layer demonstrates that the data are registered with an accuracy better than one pixel (Figure 13). However, the observed surface features are slightly displaced limbward, and the shift increases with the emergence angle in the northern direction (Figures 12a and 12b). The first version of the GTDR [*Ford and Pettengill*, 1992] (distributed by the PDS Geoscience node) is used in the archive; further refinements of the GTDR from improved Magellan orbit reconstruction [e.g., *Rappaport et al.*, 1999] do not fit better: relief locations are identical in successive versions, with differences concentrated at the sharp transitions. However, the shift disappears when the data are projected not on the ellipsoid, but on a 60 km altitude shell representing the top of the scattering atmosphere (Figure 12c). This confirms that light travels mostly in the vertical direction through the atmosphere, owing to intense scattering effects.

[82] The strong bending of light rays in the atmosphere can be described using an effective refraction index. The shift of about 4 pixels (2.5°) observed for an emergence of ~50° on the cloud top corresponds to a refractive index (at 1–1.20 μm) ranging from 1.03 to 1.04. Extrapolation of Earth's variations at Venus pressure and temperature conditions yields a value of ~1.003. The much larger value observed by VIRTIS is related to strong scattering on Venus, and perhaps to the compositional difference. Finally, the data compare in resolution with the GTDR averaged on the pixel surface and convolved with a 6 pixels box (Figure 13). This convolution kernel provides an estimate of blurring effects in the atmosphere in these particularly favorable conditions, with a PSF about 5° wide (FWHM) for an emergence of 50° (or ~1.5 airmass). The corresponding resolution at the surface is ~35 km, and is probably close to the maximum achievable with this observing technique.

4.5. Lightning

[83] Optical detection of lightning has been performed by the Venera 9 visible spectrometer [*Krasnopolskii*, 1983] then from Earth-based observations [*Hansell et al.*, 1995]. Visible spectra are roughly white, with radiance at least 4 times that of neighboring areas. Electromagnetic wave detections suggest that the activity is concentrated near the dusk limb (see review by *Russell et al.* [2006]).

[84] Electromagnetic activity is reported routinely from Venus Express, and interpreted as lightning detection [*Russell et al.*, 2007]. VIRTIS could therefore observe flashes during nighttime observations, possibly concentrated near the dusk terminator. The frequent detection of cosmic rays and other punctual features by ICA shows that lightning with a specific signature should be readily detected if present in the cubes, as long as they do not saturate the detector. "Specific" in this context may mean an unusual intensity ratio in the atmospheric windows. If lightning events have regular, simply brighter spectra, they would appear as isolated maxima on one of the main components and may be difficult to identify.

[85] So far no firm detection has been found, although not all transient events in the data set are fully understood. Because the instrument is a slit spectrometer with limited field of view, the probability of detection is also rather small. Positive detection, or even reliable statistics, may require the analysis of a large number of sessions, and this activity is still ongoing.

4.6. Limb Observations

[86] Dedicated limb sessions allow study of the upper atmosphere and its vertical profile. Although deexcitation of newly recombined O_2 is observed on the nightside, most signatures are due to fluorescence and are present only in daytime limb observations.

[87] We focus here on session 43_00, a tangential limb observation acquired at short integration time (0.36 s). This mode is adapted to long-wavelength studies, while the short wavelengths are affected by noise, by a nonlinearity pattern in the dark current, and by intense scattering. The present analysis is therefore limited to the 3.5–5.12 μm range. The data are acquired over the northern hemisphere, in the Guinevere Planitia quadrangle, entirely during day time.

[88] Even in this situation where the signal is small and concentrated on restricted locations, the actual signatures are correctly separated from the noise and artifact. The largest contributions are located below 70 km and are related to thermal emission and CO_2 absorption in the cloud layers. Two components appear to be controlled by CO_2 emission only: they dominate the signal in the 4.2–4.5 μm spectral range, and are only marginally affected by other wavelengths (Figure 14).

[89] Component 8 is the main contribution to the CO_2 complex at 4.2–4.5 μm, peaking at 4.32 μm and 4.35 μm,

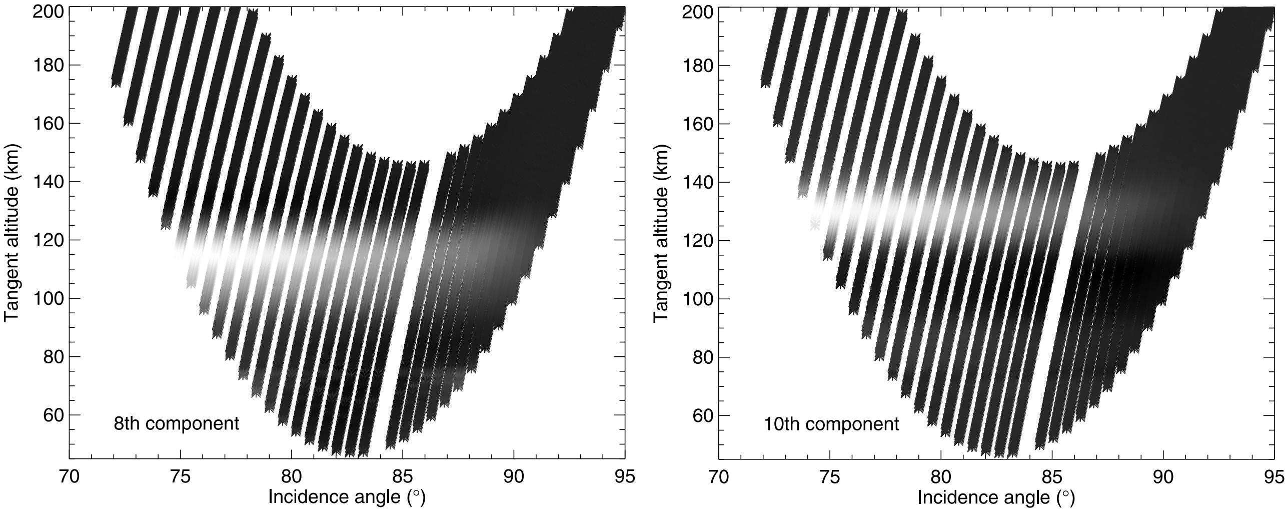

Figure 15. Coefficients for the two components in Figure 14 as a function of tangent altitude and incidence angle. Larger contributions are figured in white tones.

with a large additional contribution to the long-wavelength side of the complex, peaking at 4.44 μm (Figure 14). Component 10 is a lesser contribution (~ half of the previous one) with a distinct spectral shape peaking at 4.28 and 4.32 μm. These spectral shapes are consistent with predictions of non-LTE models ([*Lòpez-Valverde et al.*, 2007], see discussion by *Gilli et al.* [2008]).

[90] These two components are detected at latitudes in the 60°–75°N range. Figure 15 shows their distribution as a function of tangent altitude and incidence angle (i.e., solar zenith angle). The two components appear to be spatially decoupled, with the major contribution peaking at ~110 km, and the low-wavelength one at 130 km, again in agreement with theoretical predictions. The attenuation with increasing incidence angle is also predicted. These plots compare very well with the band intensity plots in the work by *Gilli et al.* [2008, Figure 7]. A third component exhibits significant variations with altitude above the 80 km level, but it includes strong thermal and absorption signatures; it more likely represents the cold collar surrounding the polar vortex at latitudes 60–75°N. Finally CO fluorescence peaking at 4.68 and 4.78 μm does not stand out clearly, but could be mixed with thermal emission in other components; it appears to be difficult to detect at the spectral resolution of VIRTIS-M. Apart from the strong, main O_2 band at 1.27 μm, other limb signatures detected with VIRTIS are very faint and require spatial summation to be identified [see *Piccioni et al.*, 2008]. Those are not identified in limb data by ICA so far.

5. Conclusions

[91] The VIRTIS-M infrared observations of the nightside and limb of Venus have been analyzed with ICA [*Cardoso*, 1999]. A methodology has been set up to minimize instrumental effects and to interpret the results.

[92] The analyses are run directly on data calibrated in radiance, with saturated pixels set to 0. Data acquired with long exposure times are analyzed in the 1.02–3.9 μm range. Isolated dead or hot pixels have minor impact on the components definition. However, two potential sources of artifact are filtered prior to analysis: spectra of the dark sky, and clusters of dead pixels. In this work, we removed the columns affected from the data cubes and maintained the complete spectral information whenever possible. This precaution results in a noticeable improvement of the analyses: the spectral components are more easily interpreted, and their spatial distributions are more consistent.

[93] The method proves to be extremely robust to noise and to large, random variations (cosmic rays). Those are for the most part isolated in specific components and do not interfere with the signal analysis. Typically, 5 to 7 components among the first 10 are related to the signal from Venus, and the others describe instrumental effects and transient events in the data. Uncalibrated instrumental effects are usually clearly identified and are decoupled from the signal in good approximation, at least in low opacity situations. In the current stage of data calibration, the main effects include irregular spectral registration along the spatial dimension of the detector, with first (gradient) and second (Laplacian) orders of deformation directly evidenced.

[94] The ICA always identifies the bulk signal from the atmosphere, modulated by the major opacity variations: zonal cloud pattern and limb darkening. Limb darkening may be detected separately whenever the cloud pattern is reduced, i.e., in situations of low opacity. The main component represents between 40 and 60% of the signal in general, but seldom introduces the largest heterogeneity between spectra. All contributions in the atmospheric windows are grouped in this component, which evidences faint, nearly opaque windows not reported before Venus Express. Such signatures are confirmed at 1.51 and 1.55 μm, with intensities ~30% and 10% of the 1.31 μm window. Besides, significant signal is measured on the longward foot of the 1.74 μm peak, up to 1.86 μm, with secondary maxima located at 1.78 and 1.82 μm.

[95] Other components are defined either through intensity balance in the main atmospheric windows (at 1.74 and 2.3 μm), or through differential detection of small signatures. In polar views, the peaks' intensity (controlled by

limb darkening) and the black body emission (with a strong maximum in the polar region) are detected together on a separate component. At high latitudes, two additional components are required to describe the main variations in the atmospheric signal: one which responds to opacity variations seen under low emergence and related to the difference of photometric functions in the long-wavelength peaks, the other one similar to branching parameter maps, and related to changing particle size distribution. The latter displays the structure of the polar vortex, which appears to be composed of two main concentric areas, with larger average particle size in the outer shell; the two shells of the vortex are composed of many concentric rings with a similar opposition at a smaller scale.

[96] Local atmospheric features are evidenced by the analysis in specific conditions. Under clear atmosphere, small-scale structures are detected separately in the cloud layers at 2.3 μm at low latitudes. They are consistent with localized evaporations of the lower/middle cloud layer, but also suggest the presence of discrete clouds about 100 km in dimension. At high latitudes, tenuous and elongated veils are observed at 1.74 μm and in the black body emission, suggesting high-altitude, warm clouds ranging from the polar vortex down to 55°S.

[97] High-altitude emission signatures from various species are correctly reported. Emission from recombined O_2 is always detected separately at 1.27 μm, in association with the much fainter 1.58 μm feature observed mostly at the limb. Limb observations show CO_2 non-LTE emission with its two characteristic signatures well separated, peaking at 110 and 130 km altitude. Other vertical variations are present at the limb, which are probably related to the thermal structure of the cloud layers and the upper atmosphere, and are still under study.

[98] For low cloud opacity, the surface is detected directly down to the minimum elevation. Under high opacity however, only the upper summits are detected through minimum radiance in the outgoing flux. This suggests that intense scattering takes place near the surface, below the summits, in some situations. This scattering at the bottom of the atmosphere is most likely related to uplifted dust. From the limited number of sessions analyzed so far, the effect seems to be present in the topographic lows of the southern hemisphere, but not over Aphrodite Terra. Spatial resolution at the surface is limited by atmosphere blurring. The maximum resolution achieved so far, in exceptional conditions, is on the order of 35 km, and is probably close to the limit. In these conditions, strong light bending is observed with an effective refraction index on the order of 1.03.

[99] This preliminary study of the VIRTIS nightside and limb observations demonstrates the power of Independent Component Analysis applied to imaging spectroscopy data of a thick atmosphere, and qualifies it to analyze spectral remote sensing data. Without any a priori assumptions, the main physical phenomena are identified and located spatially, and their relative intensities are correctly estimated. Small structures are enhanced, because the various sources of variability which affect the same spectral channels are separated, and because the signal-to-noise ratio is increased by summing all channels carrying related information. In particular, association of very faint spectral signatures are clearly evidenced (down to signal-to-noise ratios ~10 or less), thanks to the quality of the instrument and data calibration. Specific spectral signatures with limited spatial expression are also highlighted. Finally, ICA automatically performs adequate corrections to untangle the main physical phenomena, similar to empirical methods based on best-fit parameters.

[100] This "assessment study" is successful in the sense that the main regularities in the data set, studied independently by more elaborated means, are retrieved consistently with a blind source separation technique, down to low levels of variance and signal-to-noise ratio. Given minimal precautions, the method can therefore be confidently applied, at least as a quick-look tool, to large data sets produced by modern imaging spectroscopy experiments. Future, more detailed and systematic applications to VIRTIS data are expected to ease and enhance both dynamical studies (e.g., evolution of small clouds) and measurement of faint spectral features.

[101] **Acknowledgments.** The VIRTIS experiment is supported by CNES and ASI. The experiment has been built and operated by the science and technical team listed at the following address: http://servirtis.obspm.fr/Venus_Express/VIRTIS_Team.html. We gratefully thank the VIRTIS technical team for continuous and high level support as well as Bruno Bzard and Colin Wilson for constructive discussions and editorial help. The VIRTIS data archive is distributed online by ESA on the Planetary Science Archive Web site (http://www.rssd.esa.int/index.php?project=PSA&page=vexIndex).

References

Allen, D. A., and J. W. Crawford (1984), Cloud structure on the dark side of Venus, *Nature*, *307*, 222–224.

Baines, K. H., S. Atreya, R. W. Carlson, D. Crisp, P. Drossart, V. Formisano, S. S. Limaye, W. J. Markiewicz, and G. Piccioni (2006), To the depths of Venus: Exploring the deep atmosphere and surface of our sister world with Venus Express, *Planet. Space Sci.*, *54*, 1263–1278, doi:10.1016/j.pss.2006.04.034.

Cardoso, J.-F. (1999), High-order contrasts for independent component analysis, *Neural Comput.*, *11*, 157–192.

Carlson, R. W., K. H. Baines, L. W. Kamp, P. R. Weissman, W. D. Smythe, A. C. Ocampo, T. V. Johnson, D. L. Matson, J. B. Pollack, and D. Grinspoon (1991), Galileo infrared imaging spectroscopy measurements at Venus, *Science*, *253*, 1541–1548.

Carlson, R. W., L. W. Kamp, K. H. Baines, J. B. Pollack, D. H. Grinspoon, T. Encrenaz, P. Drossart, and F. W. Taylor (1993), Variations in Venus cloud particle properties: A new view of Venuss cloud morphology as observed by Galileo Near-Infrared Mapping Spectrometer, *Planet. Space Sci.*, *41*, 477–485, doi:10.1016/0032-0633(93)90030-6.

Comon, P. (1990), Analyse en composantes indépendantes et identification aveugle, *Trait. Signal*, *7*, 435–450.

Connes, P., J. F. Noxon, W. A. Traub, and N. P. Carleton (1979), O_2 ($^1\Delta$) emission in the day and night airglow of Venus, *Astrophys. J.*, *233*, L29–L32, doi:10.1086/183070.

Coradini, A., et al. (1998), VIRTIS: An imaging spectrometer for the Rosetta mission, *Planet. Space Sci.*, *46*, 1291–1304.

Drossart, P., et al. (2007a), Scientific goals for the observation of Venus by VIRTIS on ESA/Venus Express mission, *Planet. Space Sci.*, *55*, 1653–1672, doi:10.1016/j.pss.2007.01.003.

Drossart, P., et al. (2007b), A dynamic upper atmosphere of Venus as revealed by VIRTIS on Venus Express, *Nature*, *450*, 641–645, doi:10.1038/nature06140.

Erard, S. (2008), VEx-VIRTIS to planetary science archive interface control document, *Rep. VIRTIS VIR-LES-IC-2269*, Lab. dEtud. Spatiales et dInstrum. en Astrophys., Paris.

Esposito, L. W., R. G. Knollenberg, M. I. Marov, O. B. Toon, and R. P. Turco (1983), The clouds are hazes of Venus, in *Venus*, pp. 484–564, Univ. of Ariz., Tuscon.

Ford, P. G., and G. H. Pettengill (1992), Venus topography and kilometer-scale slopes, *J. Geophys. Res.*, *97*, 13,103–13,114.

Forni, O., F. Poulet, J.-P. Bibring, S. Erard, C. Gomez, Y. Langevin, B. Gondet, and the OMEGA science team (2005), Component separation of OMEGA spectra with ICA, *Lunar Planet. Sci.*, *XXXVI*, Abstract 1623.

Gérard, J.-C., A. Saglam, G. Piccioni, P. Drossart, C. Cox, S. Erard, R. Hueso, and A. Sànchez-Lavega (2008), Distribution of the O_2 infrared nightglow observed with VIRTIS on board Venus Express, *Geophys. Res. Lett.*, *35*, L02207, doi:10.1029/2007GL032021.

Gilli, G., M. A. Lopez-Valverde, P. Drossart, G. Piccioni, S. Erard, A. Cardesin, and the VIRTIS team (2008), Limb observations of non-LTE emissions in the Venus atmosphere by VIRTIS/Venus Express, *J. Geophys. Res.*, doi:10.1029/2008JE003112, in press.

Grieger, B., N. I. Ignatiev, N. M. Hoekzema, and H. U. Keller (2004), Indication of a near surface cloud layer on Venus from reanalysis of Venera 13/14 spectrophotometer data, in *Planetary Probe Atmospheric Entry and Descent Trajectory Analysis and Science*, *Eur. Space Agency Spec. Publ.*, *544*, 63–70.

Grinspoon, D. H., J. B. Pollack, B. R. Sitton, R. W. Carlson, L. W. Kamp, K. H. Baines, T. Encrenaz, and F. W. Taylor (1993), Probing Venus's cloud structure with Galileo NIMS, *Planet. Space Sci.*, *41*, 515–542, doi:10.1016/0032-0633(93)90034-Y.

Hansell, S. A., W. K. Wells, and D. M. Hunten (1995), Optical detection of lightning on Venus, *Icarus*, *117*, 345–351, doi:10.1006/icar.1995.1160.

Hashimoto, G. L., and S. Sugita (2003), On observing the compositional variability of the surface of Venus using nightside near-infrared thermal radiation, *J. Geophys. Res.*, *108*(E9), 5109, doi:10.1029/2003JE002082.

Kamp, L. W., F. W. Taylor, and S. B. Calcutt (1988), Structure of Venus's atmosphere from modelling of night-side infrared spectra, *Nature*, *336*, 360–362.

Krasnopolskii, V. A. (1983), Venus spectroscopy in the 3000–8000 region by Veneras 9 and 10, in *Venus*, pp. 459–483, Univ. of Ariz., Tuscon.

Lòpez-Valverde, M. A., P. Drossart, R. Carlson, R. Mehlman, and L. W. Roos-Serote (2007), Non-LTE infrared observations at Venus: From NIMS/Galileo to VIRTIS/Venus Express, *Planet. Space Sci.*, *55*, 1757–1771, doi:10.1016/j.pss.2007.01.008.

McGouldrick, K., and O. B. Toon (2007), An investigation of possible causes of the holes in the condensational Venus cloud using a microphysical cloud model with a radiative-dynamical feedback, *Icarus*, *191*, 1–24, doi:10.1016/j.icarus.2007.04.007.

Meadows, V. S., and D. Crisp (1996), Ground-based near-infrared observations of the Venus nightside: The thermal structure and water abundance near the surface, *J. Geophys. Res.*, *101*, 4595–4622, doi:10.1029/95JE03567.

Moudden, Y., J.-L. Starck, P. Abrial, and J.-F. Cardoso (2005), *MRS: Multi-Resolution on the sphere*, 102 pp., DAPNIA Comm. l'Energ. At., Gif-sur-yvette, France.

Moussaoui, S., H. Hauksdottir, F. Schmidt, C. Jutten, J. Chanussot, D. Brie, S. Douté, and J. A. Benediksson (2008), On the decomposition of Mars hyperspectral data by ICA and Bayesian positive source separation, *Neurocomputing*, *71*, 2194–2208.

Mueller, N., J. Helbert, G. L. Hashimoto, C. C. C. Tsang, S. Erard, G. Piccioni, and P. Drossart (2008), Venus surface thermal emission at 1 μm in VIRTIS imaging observations: Evidence for variation of crust and mantle differentiation conditions, *J. Geophys. Res.*, *113*, E00B17, doi:10.1029/2008JE003118.

Piccioni, G., et al. (2007), South-polar features on Venus similar to those near the north pole, *Nature*, *450*, 637–640, doi:10.1038/nature06209.

Piccioni, G., et al. (2008), First detection of hydroxyl in the atmosphere of Venus, *Astron. Astrophys.*, *483*, L29–L33.

Pollack, J. B., et al. (1993), Near-infrared light from Venus nightside: A spectroscopic analysis, *Icarus*, *103*, 1–42, doi:10.1006/icar.1993.1055.

Rappaport, N. J., A. S. Konopliv, A. B. Kucinskas, and P. G. Ford (1999), An improved 360 degree and order model of Venus topography, *Icarus*, *139*, 19–31, doi:10.1006/icar.1999.6081.

Russell, C. T., R. J. Strangeway, and T. L. Zhang (2006), Lightning detection on the Venus Express mission, *Planet. Space Sci.*, *54*, 1344–1351, doi:10.1016/j.pss.2006.04.026.

Russell, C. T., T. L. Zhang, M. Delva, W. Magnes, R. J. Strangeway, and H. Y. Wei (2007), Lightning on Venus inferred from whistler-mode waves in the ionosphere, *Nature*, *450*, 661–662, doi:10.1038/nature05930.

Sanchez-Lavega, A., et al. (2008), Variable winds on Venus mapped in three dimensions, *Geophys. Res. Lett.*, *35*, L13204, doi:10.1029/2008GL033817.

Schaefer, L., and B. Fegley (2004), Heavy metal frost on Venus, *Icarus*, *168*, 215–219.

Taylor, F. W., D. J. Diner, L. S. Elson, D. J. McCleese, J. V. Martonchik, J. Delderfield, S. P. Bradley, J. T. Schofield, J. C. Gille, and M. T. Coffey (1979), Temperature, cloud structure, and dynamics of Venus middle atmosphere by infrared remote sensing from Pioneer Orbiter, *Science*, *205*, 65–67.

Titov, D. V., et al. (2006), Venus Express science planning, *Planet. Space Sci.*, *54*, 1279–1297, doi:10.1016/j.pss.2006.04.017.

Wilson, C., S. Guerlet, P. G. J. Irwin, C. C. C. Tsang, F. W. Taylor, R. W. Carlson, P. Drossart, and G. Piccioni (2008), Evidence for anomalous cloud particles at the poles of Venus, *J. Geophys. Res.*, *113*, E00B13, doi:10.1029/2008JE003108.

P. Drossart and S. Erard, LESIA, Observatoire de Paris, 5 place Jules Janssen, Meudon, F-92195 France. (stephane.erard@obspm.fr)

G. Piccioni, INAF, IASF, Via del Fosso del Cavaliere 100, I-00133 Rome, Italy.